

Modelling the Propeller Slipstream Effect on the Longitudinal Stability and Control

Thijs Bouquet

Technische Universiteit Delft



MODELLING THE PROPELLER SLIPSTREAM EFFECT ON THE LONGITUDINAL STABILITY AND CONTROL

by

Thijs Bouquet

in partial fulfillment of the requirements for the degree of

Master of Science
in Aerospace Engineering

at the Delft University of Technology,
to be defended publicly on Friday January 22, 2016 at 1:30 PM.

Supervisors:	Prof. dr. ir. L. L. M. Veldhuis	
	Dr. ir. R. Vos	
Thesis committee:	Dr. ir. E. van Kampen	TU Delft

An electronic version of this thesis is available at <http://repository.tudelft.nl/>.
Thesis registration number: 069#16#MT#FPP

ACKNOWLEDGEMENTS

This thesis marks the conclusion of my time as a student at the faculty of Aerospace Engineering of Delft University of Technology. This was no small feat, which could not have been done without the help of others, I would therefore like to express my gratitude.

First of all, I would like to thank my supervisors, Dr.ir.Roelof Vos and Prof.dr.ir.Leo Veldhuis, for their guidance, support and feedback throughout the past year. Secondly, I would like to thank Dr.ir.Erik-Jan van Kampen for being a part of my thesis committee. I would also like to thank my friends and colleagues for their support. A special mention has to be made for the students of 'Kamertje-1', whose mutual goals created a sense of camaraderie which motivated me greatly.

Finally, I would like to thank my family, who were never more than a phone call away to support and encourage me throughout my entire education.

*Thijs Bouquet
Delft, January 2016*

SUMMARY

As the aviation industry continues to strive for improvements in fuel efficiency throughout the entire aircraft design, interest has been renewed in propeller engines. New research into advanced turboprop engines, so-called open rotor engines, seems promising as they combine the inherent high propulsive efficiency of ordinary turboprop engines, with the capability of delivering higher thrust.

Unfortunately, the implementation of propeller engines does have significant implications on the stability and controllability of an aircraft. These implications are primarily caused by the propeller slipstream, the complex streamtube behind the propeller with strong gradients in various flow quantities both in streamwise and radial direction. The objective of this thesis was to develop, implement, and validate a prediction method for the propeller slipstream effect on the longitudinal stability and control of conventional aircraft configurations in the Initiator.

During the investigation of the propeller slipstream effect, an existing prediction method was found which was based on calculating the four major effects caused by the propeller slipstream on the longitudinal stability and control. These four effects are, an additional normal force at the propeller disk, an increase in lift over the wing due to the slipstream, a change in the tail-off pitching moment, and a change in tail contribution to the pitching moment due to increased downwash and dynamic pressure.

This method seemed ideal as it not only gives relatively accurate results, but does so with computationally inexpensive calculations. During the implementation of this method in the Initiator, additional changes were made to calculate aerodynamic variables which were previously estimated using an extended vortex lattice method program.

This implemented prediction method was validated using the only available wind tunnel data for the Fokker 50 and a special Saab 340 with T-tail configuration. Through this validation, the prediction method proved to maintain an acceptable accuracy for all configurations with minimal computation time.

Further analysis of the results showed that the propeller slipstream effect reduces the tail effectiveness due to an increase in downwash angle at the tail. This was especially the case for the Fokker 50, which due to its low wing configuration, has a further increase in downwash caused by an inflow effect of the outer flow into the streamtube.

Interestingly, the increased downwash was shown to have a positive influence on the tested longitudinal controllability constraint which required the aircraft to pitch up. However, if the control capacity required to pitch an aircraft nose-down was examined, this would not be the case. Therefore, the complete effect of the propeller slipstream on the horizontal tail sizing needs to be further tested on all longitudinal stability and controllability constraints.

CONTENTS

List of Figures	ix
1 Introduction	1
2 Theoretical Background	3
2.1 Propeller theory	3
2.2 Propeller Slipstream Effect	5
2.2.1 Axial and swirl velocity profiles	6
2.2.2 Contraction	7
2.2.3 Installed Propeller Effects on Wing.	7
2.3 Longitudinal Stability and Control	8
2.3.1 Longitudinal Stability	9
2.3.2 Longitudinal Control.	10
3 Methodology	13
3.1 Aircraft Design Initiator	13
3.2 Propeller Methodology	14
3.2.1 Wing- and Power Loading Diagram	14
3.2.2 Engine Sizing	14
3.2.3 Fuel Weight Prediction.	16
3.3 Horizontal Tail Sizing Method.	16
3.3.1 Loading Diagram	16
3.3.2 X-Plot Methodology	17
3.4 Propeller Effects on the Longitudinal Stability and Control	18
3.4.1 Assumptions.	19
3.4.2 Propeller normal force	19
3.4.3 Tail-off lift coefficient	21
3.4.4 Tail-off pitching moment	23
3.4.5 Tail-on pitching moment	26
4 Code Implementation	33
4.1 Module Improvements	35
5 Results and Discussion	37
5.1 Results	37
5.1.1 Tail-off lift curves	37
5.1.2 Pitching moment curves	39
5.1.3 Horizontal Tail Contribution	41
5.1.4 Effect on Tail Sizing	43
5.2 Discussion	45
5.2.1 Validation	45
5.2.2 Analysis	47
6 Conclusions	51
7 Recommendations	53
A Saab 340 and Fokker 50 Dimensions	55
Bibliography	59

LIST OF FIGURES

1.1	Installed propulsive efficiency versus cruise Mach number for various engine design [1]	2
2.1	Propeller blade cross-sections	3
2.2	Schematic overview of propeller airflow [1]	4
2.3	Forces on a propeller blade segment (left figure) and the total forces and moments on a propeller (right figure)	4
2.4	Streamtube through an actuator disk [2]	4
2.5	Helical vortex system and slipstream tube generated by propeller [3]	6
2.6	Axial and swirl velocity profile along propeller blade [3]	6
2.7	Velocity variations along the stream direction [3]	7
2.8	Change in local lift coefficient due to different velocities [3]	8
2.9	Lift distribution over the wing as affected by the slipstream [3]	8
2.10	Geometric definitions, forces and moments for the longitudinal stability [4]	9
2.11	Pitching moment curve and the horizontal tail contribution [4]	10
2.12	Longitudinal equilibrium at the stall landing configuration [4]	11
2.13	Takeoff rotation [4]	11
3.1	Abstract overview of the design process [5]	14
3.2	Example Wing- and Power Loading Diagram using Fokker 50 top-level requirements and configuration	15
3.3	Example Loading Diagram [6]	17
3.4	Example Centre of Gravity Ranges Diagram [6]	17
3.5	Example X-plot [6]	18
3.6	Propeller Blades Sketch [7]	20
3.7	Velocity diagrams for a downward and upward rotating propeller blade section under an angle of attack [8]	20
3.8	Variation of lift-curve slope with aspect ratio, taper ratio, and sweepback for subsonic incompressible flow [9]	23
3.9	Illustration of the change in pitching moment due to propeller engines	24
3.10	Contributions to the tail-off pitching moment due to propeller engines	24
3.11	Chord definitions	25
3.12	Sketch of the slipstream centre line behind the wing trailing edge [10]	28
3.13	Downwash factor K_ϵ versus distance behind the wing trailing edge [10]	28
3.14	Schematic representation of the inflow effect of the external flow into the slipstream [10]	30
3.15	Change in downwash at the tailplane due to inflow into the slipstream - generalized curve	30
3.16	Tail span covered by the propeller slipstream	31
5.1	Tail-off lift curves - Saab 340	38
5.2	Tail-off lift curves - Saab 340 - Flaps 20 degrees	38
5.3	Tail-off lift curves - Fokker 50 - Flaps retracted	38
5.4	Tail-off lift curves - Fokker 50 - Flaps 16.5 degrees	38
5.5	Tail-off lift curves - Fokker 50 - Flaps 26.5 degrees	39
5.6	Tail-off lift curves - Fokker 50 - Flaps 40 degrees	39
5.7	Pitching moment curves - Saab 340	40
5.8	Tail-off Pitching moment curves - Fokker 50	41
5.9	Horizontal tail pitching moment - Saab 340	42
5.10	Horizontal tail pitching moment - Fokker 50	43
5.11	Horizontal tail pitching moment - Fokker 50	43
5.12	X-Plot results for the Saab 340	44

5.13 X-Plot results for the Fokker 50	44
A.1 Saab 340 dimensions	56
A.2 Fokker 50 dimension	57

LIST OF SYMBOLS

α_0	Zero lift angle of attack
α_{in}	Inflow angle at propeller disk
α	Angle of attack
$\bar{\beta}$	Average blade chord
\bar{c}	Mean aerodynamic chord
\bar{V}_h	Tail volume coefficient
β	Blade angle at .75 radius blade station
$\Delta\alpha_{0,f}$	Change in zero-lift angle of attack due to flap deflection
δ_f	Flap deflection
δe	Elevator deflection
Δh^*	The vertical displacement of the slipstream centre line due to the propeller axis not coinciding with the streamline leading to the forward stagnation point
Δh_e	The vertical displacement of the slipstream centre line passing through the clean wing's trailing edge
Δh_l	The vertical displacement of the horizontal tail due to angle of attack
ΔV	Increase in velocity in the fully contracted slipstream
\dot{m}	Mass flow
η_j	Propulsive efficiency
η	Tailplane effectiveness
η_e	Number of engines
$(\Delta\epsilon)_{\frac{\Delta V}{V_0}=1}$	Increase in downwash due to the inflow effect
ω	Angular velocity
SM	Stability Margin
σ_e	Effective propeller solidity
ϵ	Downwash angle
A	Propeller disk area
a	Axial velocity factor
a	Speed of sound
A_S	Aspect ratio of the slipstream section of the wing
A_W	Aspect ratio of the wing
b	Span

c	Wing chord
c'	Extended chord
C_D	Drag coefficient
c_f	Flap chord
C_L	Lift coefficient
C_m	Pitching moment coefficient
C_N	Propeller normal force coefficient
c_p	Specific fuel consumption
C_T	Thrust Coefficient
$C_{L\alpha}$	Lift curve slope
C_{L_R}	Takeoff lift coefficient
$C_{m_{0,s}}$	Zero-lift pitching moment coefficient of the slipstream section of the wing
$C_{m_{s,0}}$	Pitching moment due to propeller slipstream and zero angle of attack
D	Diameter
d	Diameter
D^*	Contracted propeller slipstream diameter
h_t	The geometrical distance between the tail surfance and the propeller axis at zero angle of attack
h_{tot}	Vertical distance between slipstream centre line and horizontal tail
i	Incidence angle
K_ϵ	Downwash factor
L	Lift
l	Moment arm
M	Mach number
m	Mass
n	Revolutions per second
P	Power
p	Pressure
P_{in}	Power input
P_{out}	Power output
q	Dynamic pressure
R	Range
r	Radius
ρ	Density
S	Wing surface area

T	Thrust
T'_c	Thrust coefficient based on free-stream velocity and propeller disk area
V_0	Velocity of the undisturbed flow
v_a	Axial velocity in the propeller slipstream
V_e	Increased velocity far downstream in the propeller slipstream
V_R	Rotation speed
V_S	Takeoff speed
v_t	Swirl velocity in the propeller slipstream
W	Aircraft Weight
X	Distance along longitudinal aircraft axis
Y	Distance along lateral aircraft axis
Z	Distance along vertical aircraft axis

Subscripts

$.3\bar{c}$	0.3 chord point of the mean aerodynamic chord
α	Differentiated w.r.t. angle of attack
$\bar{c}/4$	Quarter-chord point of the mean aerodynamic chord
gear	Main landing gear
prop	Propeller
$A - h$	Aircraft less tail
ac	Aerodynamic centre
$C_L = 0$	Zero lift
CG	Centre of gravity
h	Horizontal tail
n	Neutral point
P	Propeller normal force
$P - O$	Power-off condition
r	Aircraft
S	Propeller Slipstream
$T - O$	Tail-off
W	Wing
$W + S$	Wing and propeller slipstream

1

INTRODUCTION

Throughout all of society an increasingly strong focus is being placed on reducing the negative impact humans have on the environment. This is no less the case in the aviation industry, where each sector is continuously looking to reduce its environmental impact. This is especially the case in aircraft design, as innovations made within the design of an aircraft can have drastic effects on the fuel consumption of said aircraft.

Within aircraft design, large improvements can still be made in the propulsion department. Research into propeller, or open rotor, engines is showing promising results. As can be seen in Figure 1.1, especially for Mach numbers up to 0.7 turboprops are much more efficient than the more common turbofan engines. Furthermore, novel advanced turboprop engines are able to deliver this same high efficiency at even higher Mach numbers up to 0.85. Due to this higher efficiency at lower Mach numbers, turboprop and open rotor engines are proving to be a very feasible option for regional aircraft.

The implementation of these propeller engines does however have significant implications on the stability and controllability of an aircraft. Due primarily to the increased flow velocity over the wing and a propeller normal force, the pitching moments change when under the influence of a propeller slipstream. Furthermore, the increasing downwash and potential increase in dynamic pressure over the tail also changes the effectiveness of the horizontal tail. These changes must be taken into account to accurately determine the minimal horizontal tail surface area. Unfortunately, the complex nature of the propeller slipstream effect means that these implications are normally not incorporated in the conceptual design phase. As Phillips [11] says, "The effects of the propeller slipstream on other airplane surfaces such as the wing, tail and fuselage are very complex and do not lend themselves to accurate analytical treatment. These effects can be accurately evaluated only from powered wind tunnel tests. Such tests are commonly performed in the final phase of the airplane design process. Simply because of complexity, the slipstream effects are usually neglected in the preliminary design phase. It should be remembered, however, that the slipstream effects can be significant.". This leads to the main research question of this thesis:

How can the propeller slipstream effect on the longitudinal stability and control of a conventional aircraft be predicted quickly during the preliminary design phase?

The objective of this thesis project is to develop, implement, and validate a prediction method for the propeller slipstream effect on the longitudinal stability and control of conventional aircraft configurations in the Initiator. The Initiator is a conceptual design tool developed at the department of Flight Performance and Propulsion at the TU Delft. The Initiator already contains a horizontal tail sizing method. Therefore, the prediction method was written in a way that it can be incorporated within this method. Furthermore, as this is the first work done on propeller engines within the Initiator, the engine and aircraft sizing as a result of propeller engines were also implemented.

The thesis is structured as follows. The relevant theory regarding propeller engines, the slipstream effect and longitudinal stability and control is explained in Chapter 2. The implemented slipstream prediction method and aircraft sizing based on propeller engines is detailed in Chapter 3. The intended implementation of the

written code is given in Chapter 4. The results obtained to validate the prediction method and indicate the influence of the slipstream on the stability and control are presented in Chapter 5. Finally, the conclusions and recommendations following from this thesis project are given in Chapter 6 and Chapter 7 respectively.

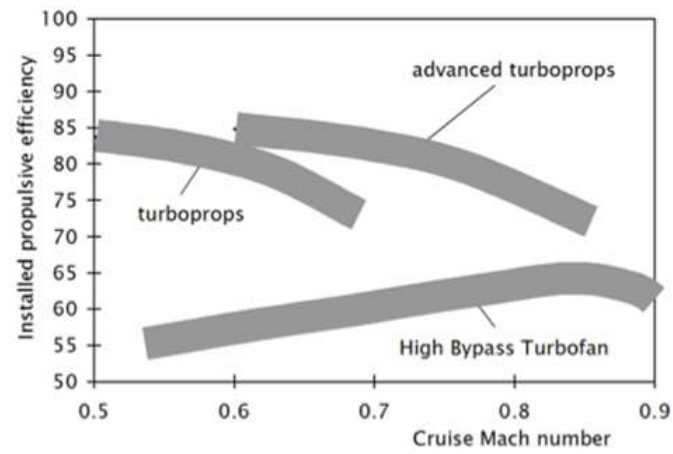


Figure 1.1: Installed propulsive efficiency versus cruise Mach number for various engine design [1]

2

THEORETICAL BACKGROUND

This chapter aims to present a brief overview of the theoretical background required to describe the methodology and results of this thesis work. The theory presented in this chapter includes the working principles of propeller engines in Section 2.1, a description of the propeller slipstream effect in Section 2.2 and finally a description of the longitudinal stability and control of an aircraft in Section 2.3.

2.1. PROPELLER THEORY

This section describes propeller engines, including their working principle, forces involved, and efficiency. The working principle behind propeller engines is similar to that of an aircraft wing. Each propeller blade cross-section is in essence an airfoil, as shown in Figure 2.1, and generates thrust in the same way that wing airfoils generate lift. By adding momentum to the airflow through the propeller, thrust is generated. Behind the propeller, a streamtube, called the propeller slipstream, is deflected over a downwash angle, creating thrust and swirl. This is shown schematically for a single propeller blade segment in Figure 2.2.

The forces acting on a single blade element are shown in Figure 2.3. These are the resultant R , which is split into the thrust T and torque P . The equivalent lift and drag forces are also shown to clearly indicate the similarity with a wing airfoil. The relevant velocities at the blade element are also shown. These are the forward flight velocity V_∞ , the tangential velocity ωr , and the resultant velocity V , giving an effective angle of attack α_{eff} . The resulting total forces and moments on a propeller engine are also shown in Figure 2.3. The main contributing force acting on the propeller is the thrust, however the normal force will also be very important for this thesis as it has a significant effect on the stability of the aircraft.

To further explain the basics of propeller engines, an incompressible momentum theory presented by Roskam [2] is used. In this theory, the propeller disk is replaced by a disk consisting of an infinite number of uniformly loaded propeller blades, called an actuator disk. The airflow through this disk is then assumed to be incompressible and irrotational. This gives the situation as illustrated in Figure 2.4.

By applying the incompressible Bernoulli equation to the situation illustrated

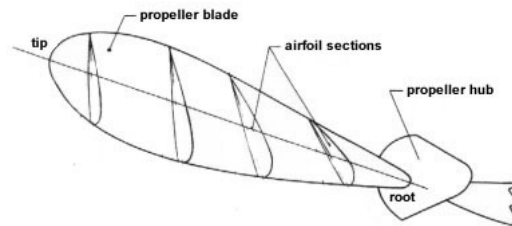


Figure 2.1: Propeller blade cross-sections

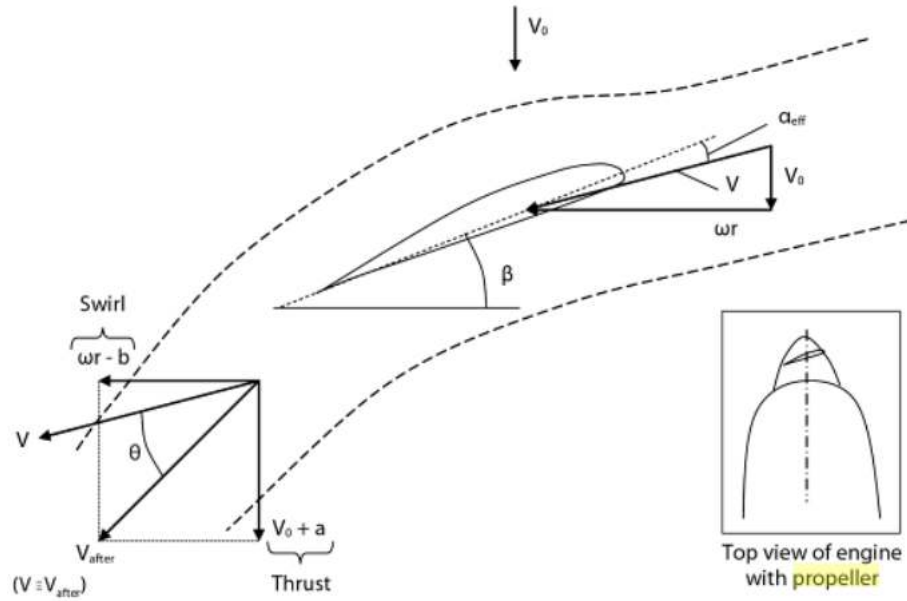


Figure 2.2: Schematic overview of propeller airflow [1]

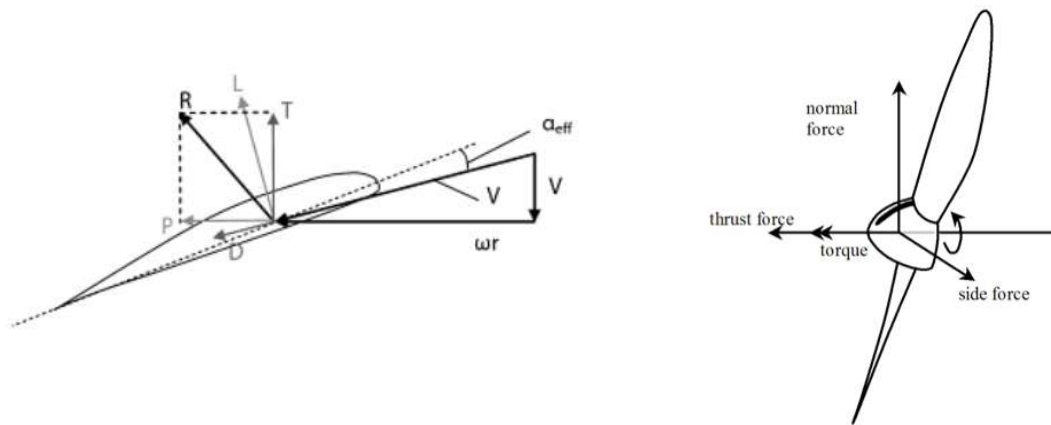


Figure 2.3: Forces on a propeller blade segment (left figure) and the total forces and moments on a propeller (right figure)

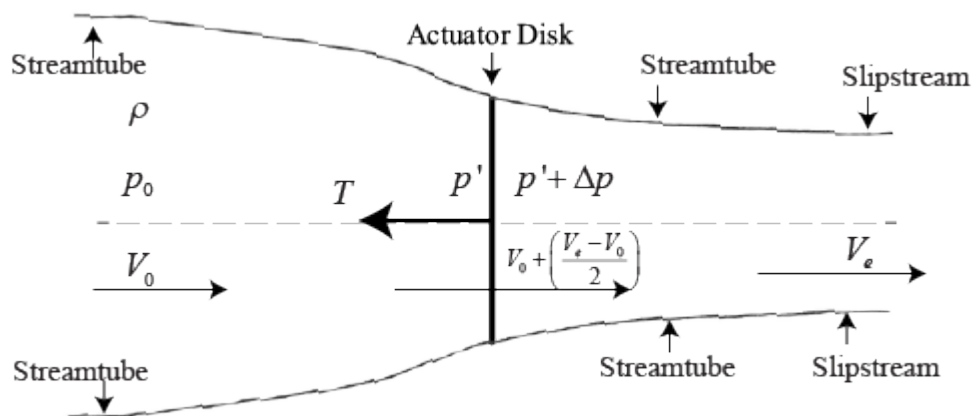


Figure 2.4: Streamtube through an actuator disk [2]

in the figure, the thrust produced by the propeller is found to be:

$$T = A\Delta p = A\rho \left(V_0 + \frac{V_e - V_0}{2} \right) V_e \quad (2.1)$$

Where A is the propeller disk area, V_0 is the velocity of the flow upstream, and V_e is the increased flow velocity far downstream of the propeller disk. From this, it follows that the propeller thrust is strongly dependent on the velocity of the aircraft. Instead of thrust, a propeller engine is rated with respect to power. The power output of a propeller is defined as:

$$P_{\text{out}} = T V_0 \quad (2.2)$$

The power input by the engine (not accounting for losses) is defined as the thrust caused by the air pressure over the propeller disk, multiplied by the flow velocity through the disk, or:

$$P_{\text{in}} = T \left(V_0 + \frac{V_e - V_0}{2} \right) \quad (2.3)$$

Adding these two equations together gives the ideal propulsive efficiency:

$$\eta_{\text{prop}} = \frac{P_{\text{out}}}{P_{\text{in}}} = \frac{2}{1 + \frac{V_e}{V_0}} \quad (2.4)$$

From this equation, it follows that to maximize the propulsive efficiency, the velocity increase over the propeller disk must be minimal. According to Obert [10], the velocity ratio can be calculated using:

$$\frac{(V_e - V_0)}{V_0} = \sqrt{1 + C_T \frac{S}{n_e A}} - 1 \quad (2.5)$$

This means, that to maximize the propulsive efficiency by minimizing the velocity increase over the propeller disk at a certain thrust coefficient, the propeller disk area must be maximized. Unfortunately, large propeller disk areas are undesirable for three reasons [2]:

- Large diameters tend to cause high tip speeds which lead to compressibility effects
- Large diameters tend to cause ground clearance problems
- Large diameters tend to introduce structural problems with the propeller blades (high stress)

As a result, propeller diameters are limited by these three constraints. In practice, the limiting factor is found to be the tip speed. In Section 3.2.2, the implemented method for the propeller sizing based on the tip speed is presented.

2.2. PROPELLER SLIPSTREAM EFFECT

The propeller slipstream is a complex phenomenon with varying properties, all of which combine to create a helical vortex system called the slipstream tube. The work of Veldhuis [3] helped during this thesis to give an understanding of the phenomenon. The description given of the relevant properties of the propeller slipstream effect is based on his work [3].

To start, a basic representation of a propeller slipstream tube is shown in Figure 2.5. This figure illustrates the helical vortex system resulting from a propeller blade advancing through the flow. The helical vortex system tends to deform and roll-up, producing a slipstream tube with strong variations in flow quantities. Although the slipstream can be described using many variables, only the following variables will be discussed in further detail as these are relevant for the completed thesis work:

- Axial and swirl velocity profiles
- Contraction
- Installed propeller effects on the wing

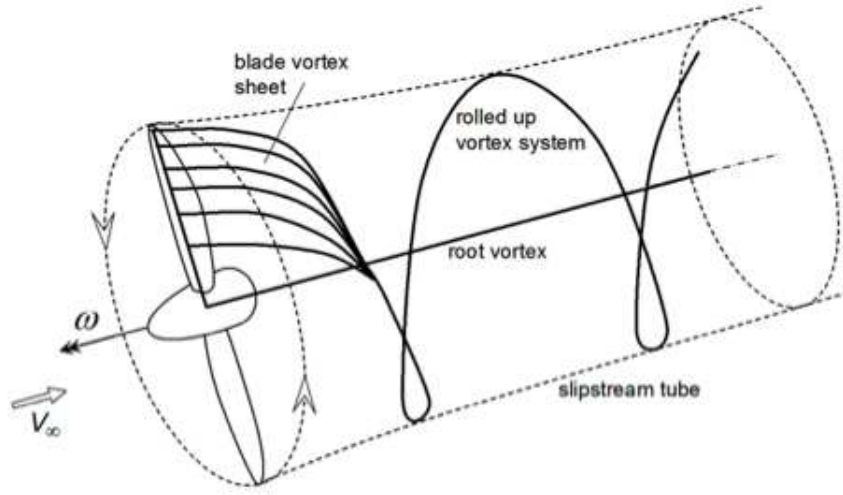


Figure 2.5: Helical vortex system and slipstream tube generated by propeller [3]

It should be noted at this point that some very significant assumptions were made to ensure the implemented prediction method remains computationally inexpensive. These assumptions are listed in Section 3.4.1.

2.2.1. AXIAL AND SWIRL VELOCITY PROFILES

When examining velocity profiles of an uninstalled propeller, the axial velocity (v_a) is determined as the velocity along the propeller thrust axis. As can be seen in Figure 2.6, the axial velocity varies along the propeller blade, with a maximum at roughly 3/4 of the radius. The maximum occurs at this position as the blade loading is also maximum at this location. Figure 2.7a shows that the axial velocity increases further along the streamwise direction. This means that the x-location of the propeller has an important influence on the axial velocity at a certain position along the streamtube.

The swirl velocity (v_t) is the propeller induced tangential velocity. The swirl velocity profile along the propeller blade can be seen in Figure 2.6. The profile varies significantly more compared to the axial profile. The swirl velocity profile in the x-direction is shown in Figure 2.7b.

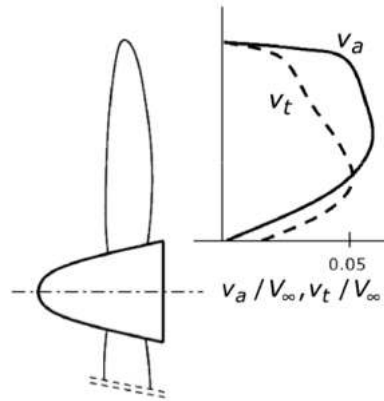


Figure 2.6: Axial and swirl velocity profile along propeller blade [3]

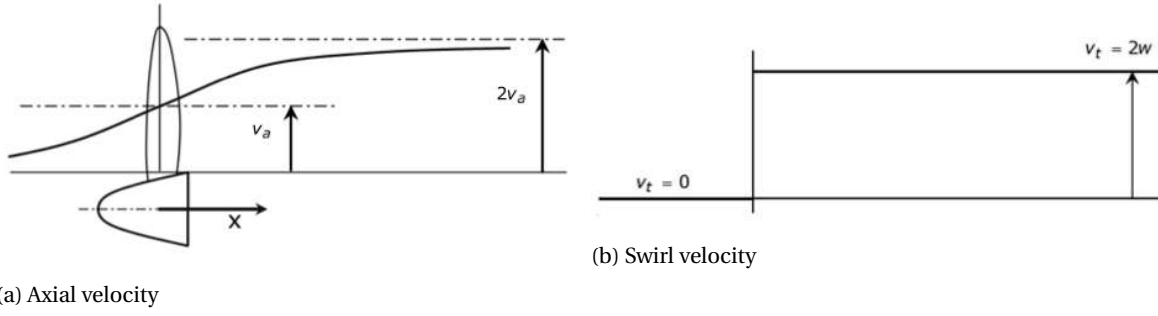


Figure 2.7: Velocity variations along the stream direction [3]

2.2.2. CONTRACTION

To fully determine the streamtube characteristics, its dimensions and shape must also be known. For the uninstalled propeller, the streamtube is assumed to be circular with the same radius as the propeller at the propeller location. Further downstream however, the streamtube contracts to maintain constant mass flow as the axial velocity increases. For the uninstalled propeller, the contraction ratio R_s/R can be approximated using equation 2.6 as determined by Theodorsen [12]:

$$\frac{R_s(x)}{R} = \sqrt{\frac{1+a}{1+a\left(1+\frac{x}{\sqrt{R^2+x^2}}\right)}} \quad (2.6)$$

Where a is defined as the dimensionless axial velocity factor $\left(\frac{v_a}{V_0}\right)$.

2.2.3. INSTALLED PROPELLER EFFECTS ON WING

The installed propeller effects on the wing are best described visually using Figures 2.8a, 2.8b, and 2.9. These figures show the direct effect that the propeller slipstream has on the wings.

Starting off with Figure 2.8a, this figure illustrates the change in local lift coefficient as a result of the axial velocity increase over the slipstream region. As the flow is accelerated due to the rotating propellers, the dynamic pressure over the wing is increased, resulting in an increase in local lift. As mentioned earlier in Subsection 2.2.1, the axial velocity profile is not uniform along the propeller blade. As a result the increase in dynamic pressure is also not uniform, but has a maximum at roughly 3/4 of the propeller blade radius for both the upward and downward rotating blade locations.

Figure 2.8b illustrates the effect of propeller rotation. As the propeller rotates, the upward rotating blade position causes an increase in local angle of attack on the wing resulting from the swirl velocity. In the same manner, the downward rotating blade position produces a lower local angle of attack on the wing. This change in local angle of attack causes a respective increase or decrease in local lift coefficient as shown in the figure. Again, as was mentioned in Subsection 2.2.1 the swirl velocity profile is not uniform along the propeller blade and as a result, the local lift coefficient is not uniform but has a maximum at roughly 3/4 of the blade radius. The importance of rotation direction is also shown by illustrating the placement of the local lift coefficient peak at the upward rotating side in the inboard or outboard rotating case.

Finally, Figure 2.9 shows how the effects of Figures 2.8a and 2.8b combine and how the regions next to the slipstream section of the wing are affected.

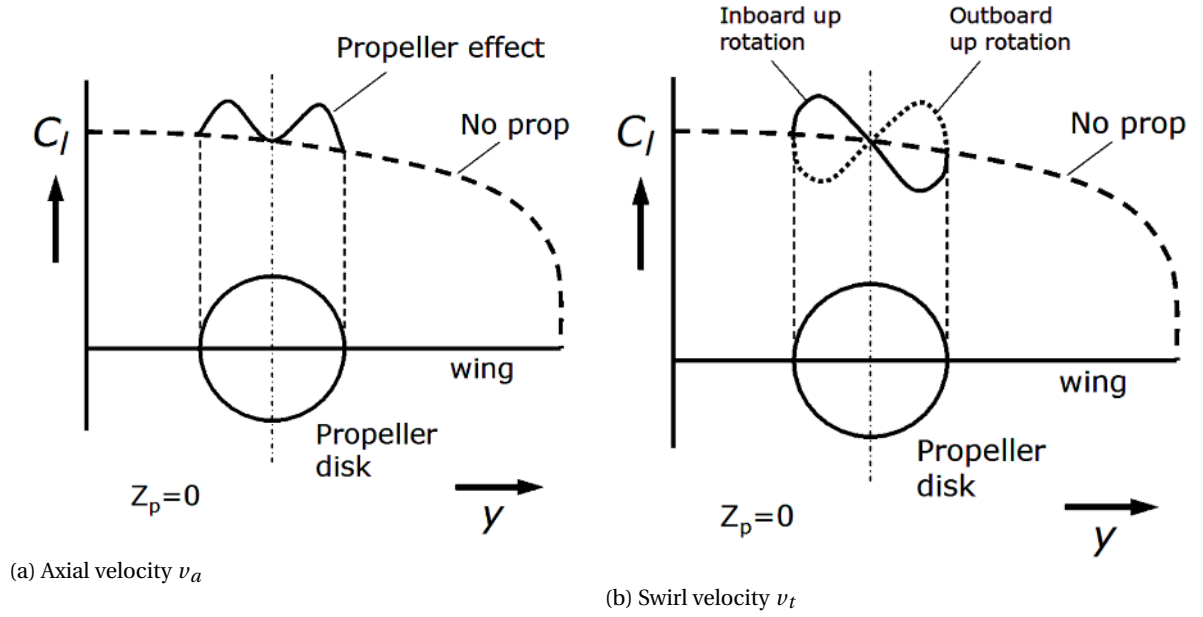


Figure 2.8: Change in local lift coefficient due to different velocities [3]

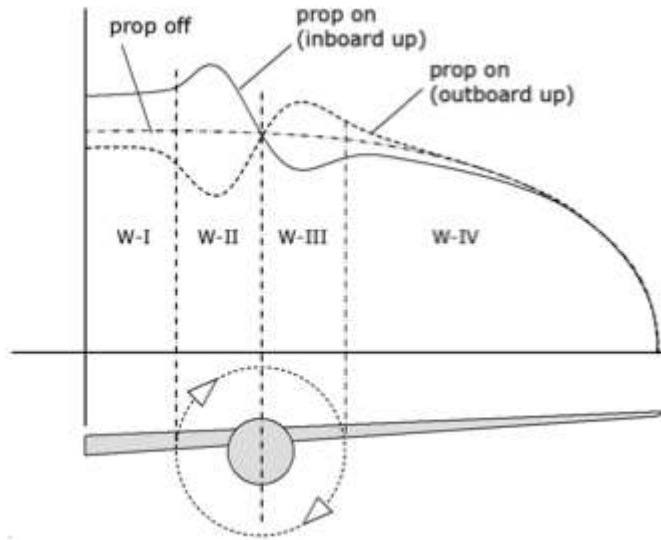


Figure 2.9: Lift distribution over the wing as affected by the slipstream [3]

2.3. LONGITUDINAL STABILITY AND CONTROL

The main objective of this thesis is to develop and implement a prediction method for the propeller slipstream effect on the longitudinal stability and control of conventional aircraft. This means it is important to have a clear understanding of what sufficient longitudinal stability and control entails. In the Initiator, an aircraft is considered longitudinally stable and controllable if it can be trimmed and is controllable at any point in its flight envelope.

The stability of an aircraft is closely tied to the position of the centre of gravity of the aircraft and the neutral point. The neutral point is the location on which the total lift force acts. An aircraft is neutrally stable if the centre of gravity coincides with the neutral point. A neutrally stable aircraft which undergoes a minor change in pitch does not restore to its original orientation or move further away from its original orientation.

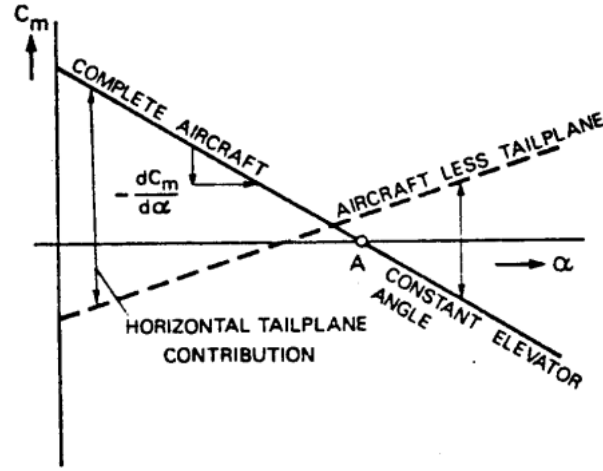


Figure 2.11: Pitching moment curve and the horizontal tail contribution [4]

neutral point is the position of the centre of gravity for which:

$$\frac{dC_m}{d\alpha} = 0 \quad (2.8)$$

For an aircraft to restore to its original state of equilibrium following a disturbance in angle of attack, it must provide an opposite pitching moment to the change in angle of attack. This means that the condition for static stability of an aircraft can be described mathematically as:

$$\frac{dC_m}{d\alpha} < 0 \quad (2.9)$$

The contribution of the tail to the pitching moment is shown in Figure 2.11. This figure shows the pitching moment curve for an aircraft without tail and for a complete aircraft. The trimmed condition is also illustrated in this figure as point A. In point A, the pitching moment coefficient (C_m) is zero and any disturbance in angle of attack causes a restorative pitching moment back to the trimmed condition A. The contribution of the horizontal tail is dependent on a number of variables such as the tail area (S_h), the moment arm of the tail (l_h), the velocity of the airflow at the tail (V_h) and the downwash angle (ϵ). The neutral point can be related to the aerodynamic centre using these variables as follows:

$$\frac{x_n - x_{ac}}{\bar{c}} = \frac{C_{L_{h\alpha}}}{C_{L_\alpha}} \left(1 - \frac{d\epsilon}{d\alpha} \right) \frac{S_h l_h}{S \bar{c}} \left(\frac{V_h}{V} \right)^2 \quad (2.10)$$

By implementing a minimum distance between the neutral point and the most aft centre of gravity, called the static margin, longitudinal stability is ensured. Using the static margin, the most aft centre of gravity limit for a certain tail size and location can be found using:

$$\frac{x_{cg}}{\bar{c}} = \frac{x_{ac}}{\bar{c}} + \frac{C_{L_{h\alpha}}}{C_{L_\alpha}} \left(1 - \frac{d\epsilon}{d\alpha} \right) \frac{S_h l_h}{S \bar{c}} \left(\frac{V_h}{V} \right)^2 - SM \quad (2.11)$$

Where:

$$SM = \frac{x_n - x_{cg}}{\bar{c}} \quad (2.12)$$

2.3.2. LONGITUDINAL CONTROL

The longitudinal control of an aircraft is also related to the distance between the neutral point and centre of gravity. However, whilst the stability requirements impose limitations on the aft centre of gravity, the controllability requirements impose limitations on the forward centre of gravity. As a result, the maximum allowable centre of gravity range is determined by finding the most dominant aft centre of gravity position due to stability, and the most dominant forward centre of gravity position due to controllability. The controllability constraints that will be examined in this thesis are the control capacity required during stall conditions, and

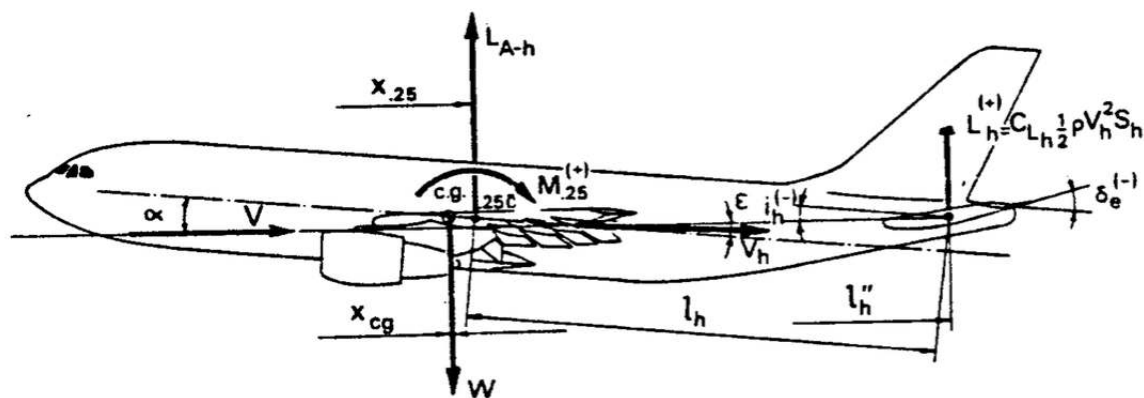


Figure 2.12: Longitudinal equilibrium at the stall landing configuration [4]

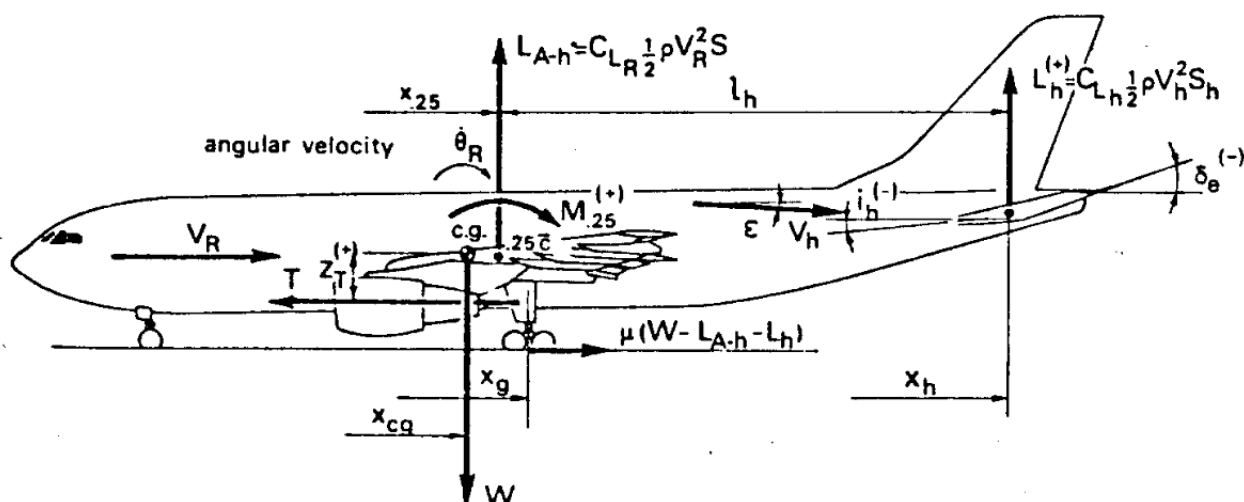


Figure 2.13: Takeoff rotation [4]

the control capacity required to ensure a minimum angular rotation velocity during takeoff.

The control capacity required to stall the aircraft ensures that the aircraft is capable of pitching up and reaching the maximum angle of attack with full flaps deflected and the centre of gravity in the most forward position. This flight situation is illustrated in Figure 2.12. The most forward centre of gravity position allowed by this constraint depending on a horizontal tail size and location is found using [4]:

$$\frac{x_{cg}}{\bar{c}} = \frac{x_{\bar{c}/4}}{\bar{c}} - \frac{1}{C_{L_{max}}} \left(C_{L_h} \frac{S_h l_h}{\bar{c} S} \frac{V_h}{V} - C_{m_{\bar{c}/4}} \right) \quad (2.13)$$

3

METHODOLOGY

In this chapter, the methodology used to predict the propeller slipstream effect on the longitudinal stability and control during the conceptual design phase will be detailed. This chapter is structured in four sections. First, a brief introduction is given to the Initiator design tool, within which this prediction method is implemented, in Section 3.1. Secondly, the changes made to the Initiator to include propeller engines are presented in Section 3.2. Thirdly, the existing horizontal tail sizing methodology for turbofan engines is explained in Section 3.3. Finally, the propeller slipstream prediction method is detailed in Section 3.4.

3.1. AIRCRAFT DESIGN INITIATOR

The Aircraft Design Initiator is a software design tool written in MATLAB, with the goal of quickly conceiving realistic aircraft designs to investigate the effect of new technologies and aircraft configurations [13]. This goal is achieved by combining empirical and numerical models, leading to accurate results with a minimal computation time. The original version of the Initiator was written by Langen [14] as a conceptual design tool for conventional and boxwing aircraft. This version was rewritten by Elmendorp [5] as a modular design tool. In doing so, the tool can easily be extended by editing or adding additional modules, rather than the entire program. This allows multiple programmers to expand the tool without interfering with one another.

Since the completion of Elmendorp's work, the Initiator has been improved by implementing more accurate analysis modules or adding aircraft configuration options. However, the overall design process has remained the same. This design process is illustrated in Figure 3.1, which was created by Elmendorp [5]. As can be seen from this figure, the process starts by establishing the top-level requirements and the aircraft configuration as inputs. These inputs are then used to carry out a Class I weight estimation.

Using the results from this weight estimation, the wing loading and thrust-to-weight ratio are determined using constraints based on regulations or performance. With the thrust-to-weight ratio and wing loading known, the geometry estimation module sizes the various aircraft parts and positions them.

A class II weight estimation based on Raymer [15] then gives weights per aircraft part based on empirical data and a centre of gravity estimation, which will prove to be vital for the horizontal stability estimation as described in Section 3.3. The Class II weight estimation is followed by aerodynamic analysis modules which can be used to resize certain aircraft parts and serve as inputs for the Class II.V weight estimation.

The Class II.V weight estimation uses aerodynamic inputs to run physics based weight estimations, such as EMWET developed by Elham [16] to more accurately determine the aircraft weight. This process is run iteratively until the Class II.V weight estimation converges. When this weight converges, a performance estimation is carried out to check whether the aircraft design can cope with the initial performance requirements. If this is not the case, the fuel mass is changed and the entire design loop is repeated until the performance requirements are met.

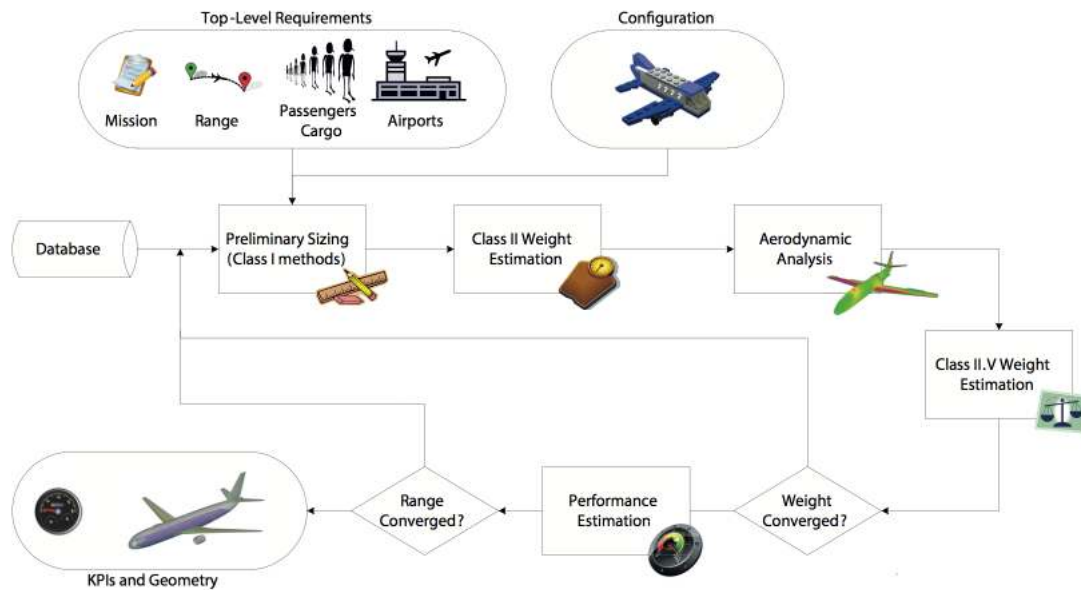


Figure 3.1: Abstract overview of the design process [5]

3.2. PROPELLER METHODOLOGY

At the start of this thesis, the Initiator primarily focussed on turbofan-powered aircraft. Which meant that before the propeller slipstream effect could be investigated, changes had to be made to incorporate aircraft configurations with turboprop engines. This section aims to describe the changes made to the Initiator to give a feasible aircraft design using propeller engines.

As can be understood from Section 2.1, the influence of propellers on aircraft design is rather significant, and fully implementing propeller engine design in the Initiator is outside the scope of this thesis. As such, assumptions and empirical methods have been used during the implementation. In the recommendations in Chapter 7, note will be made of potential improvements to the implementation.

3.2.1. WING- AND POWER LOADING DIAGRAM

The first relevant step in the Initiator design loop for the propeller implementation is the wing- and power loading diagram. This diagram, an example of which is shown in Figure 3.2, gives the optimal design point for an aircraft based on various performance and regulatory constraints. According to this diagram, the design point in this case is limited by the maximum landing distance and the required power loading to meet the required climb gradient during a balked landing (FAR 25.119). All of the performance and regulatory constraints are dependent on the engine type as propeller engines are sized based on power rather than thrust and the constraints must reflect this.

Luckily, the wing- and power loading diagram was already implemented for turboprop engines by Slingerland. The method used by Slingerland is based on the first book of Roskam [17]. As a result, no major changes were needed in this stage within the module. However, as this is the starting point of the turboprop implementation, it is vital to mention it here.

3.2.2. ENGINE SIZING

Following the wing- and power loading diagram, a geometry estimation is carried out for the various aircraft parts, including the engine. For the engine geometry, an initial attempt was made to build a database from existing turboprop engines in use on conventional commercial aircraft found in Jane's All the World's Aircraft [18]. Unfortunately, using this database, no clear relation could be established between required engine power and the various engine dimensions.

Moving away from this database, empirical relations were found by Raymer [15] which can be used to de-

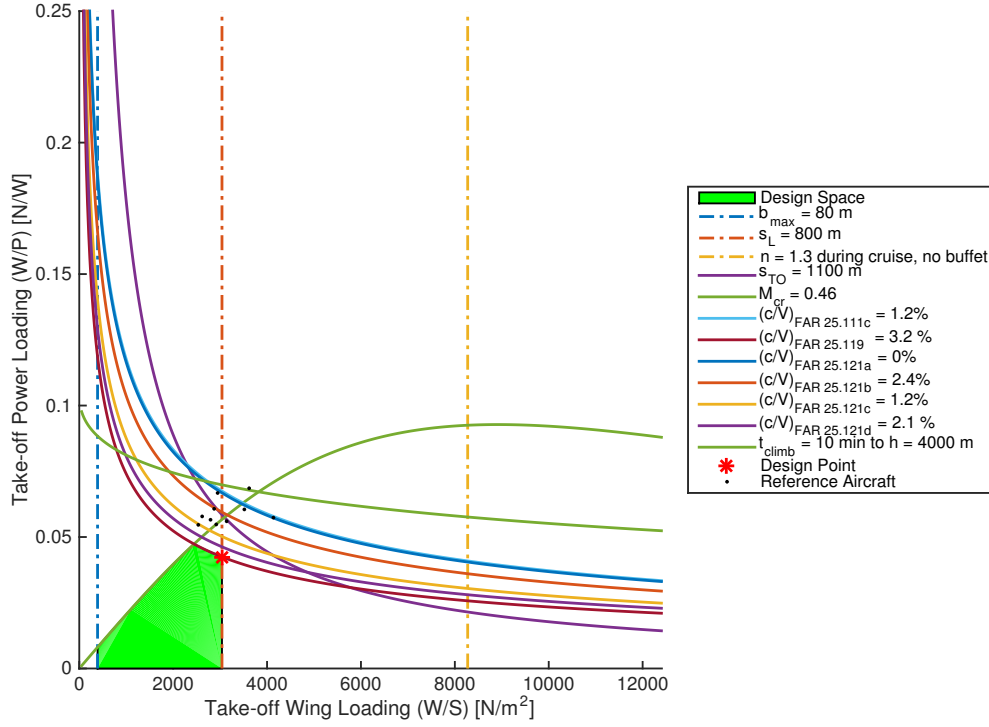


Figure 3.2: Example Wing- and Power Loading Diagram using Fokker 50 top-level requirements and configuration

termine the engine diameter and length as a function of the required engine power as shown respectively:

$$d_{\text{engine}} = 0.25 \left(\frac{P_{\text{engine}}}{1000} \right)^{0.12} \quad (3.1)$$

$$l_{\text{engine}} = 0.12 \left(\frac{P_{\text{engine}}}{1000} \right)^{0.373} \quad (3.2)$$

The uninstalled engine mass is also computed using Raymer's empirical relations as shown below. This uninstalled engine mass is scaled by a constant factor of 1.3 to give the installed engine mass as part of the Class II Weight Estimation.

$$m_{\text{uninstalledengine}} = 0.96 \left(\frac{P_{\text{engine}}}{1000} \right)^{0.803} \quad (3.3)$$

The final important dimension is the propeller diameter. As a full propeller design method is outside of the scope of this thesis, the propeller is sized purely in terms of diameter. The diameter is limited by the maximum propeller tip speed (M_{tip}^2) as stated by Roskam [2] through:

$$d_{\text{prop}} = \sqrt{\frac{a^2}{\pi^2 n^2} (M_{\text{tip}}^2 - M^2)} \quad (3.4)$$

In this equation, the maximum tip speed is equal to 0.8 by default as losses due to compressibility become too large at this point. This value can also be set to 0.72 due to acoustic constraints [2].

The blade chords which are required as part of the propeller normal force calculation in Section 3.4.2 have been set as inputs. Further work could lead to the implementation of a more elaborate propeller sizing method, perhaps by making an XRotor [19] extension. This will be elaborated in the Recommendations in Chapter 7.

3.2.3. FUEL WEIGHT PREDICTION

In the class II weight estimation, the fuel weight is determined by the Brequet range equation for turboprop engines [20]:

$$R = \frac{\eta_j}{c_p} \frac{C_L}{C_D} \ln \frac{W_1}{W_2} \quad (3.5)$$

In this equation, the propulsive efficiency (η_j) has been assumed to be a constant value. In the class II.V weight estimation however, the entire mission is simulated to calculate the fuel consumption at each point during the flight. In this case, assuming a fixed efficiency reduces the accuracy immensely. Instead, the ideal propulsive efficiency, based on flight parameters such as the thrust and flight velocity, is used [21]:

$$\eta_{\text{ideal}} = \frac{2}{1 + \sqrt{\frac{T}{A_{\text{disk}} V_0^2 \frac{\rho}{2}} + 1}} \quad (3.6)$$

During the propeller implementation work of this thesis, it was discovered that Joris van Bogaert [22] was also working on propeller implementation within the Initiator. After having a meeting to compare our respective work, we noted that up until this point we had implemented propellers following almost the exact same method. However, the work of van Bogaert was focused on fuel consumption. This meant that he would carry on implementing a model to predict the fuel consumption based on the variation of specific fuel consumption with respect to velocity and altitude. Therefore, during the code implementation described in Chapter 4, the work of van Bogaert [22] will be implemented for the fuel weight prediction in the Class II.V weight estimation. Unfortunately this means that the code that was written as part of this thesis for the fuel prediction will most likely not be implemented.

3.3. HORIZONTAL TAIL SIZING METHOD

To give a clear understanding of the effects of propeller implementation on the longitudinal stability and control, it is important to first give a brief description of the existing *@HorizontalStabilityEstimation* module. As mentioned earlier, this module was created by Quinten Jansen [6]. This section is written to ensure the reader has an understanding of where the propeller effects calculated in the next section are incorporated within the design process. Should the reader wish for a more thorough explanation of the *HorizontalStabilityEstimation* module, the thesis work by Jansen [6] should be consulted. At this point it should be noted that the module was reviewed and improved as a part of this thesis. Unfortunately, this work proved to be quite laborious and another master student took over the remaining work. At the point of writing this thesis, the work has not completed and as a result, the propeller slipstream method will be implemented in the module at a later date.

The description of the existing *HorizontalStabilityEstimation* module will be split into two parts. First, the method for determining the minimum centre of gravity range for which the horizontal tail must provide sufficient longitudinal stability and control is explained in Subsection 3.3.1. Secondly, the X-plot method used to relate the minimum horizontal tail surface area to the centre of gravity range is detailed in Subsection 3.3.2.

3.3.1. LOADING DIAGRAM

To determine the minimum centre of gravity range for which the aircraft must remain longitudinally stable or controllable, a loading diagram is computed. A loading diagram, an example of which is shown in Figure 3.3, indicates all the possible centre of gravity positions for a certain aircraft. The variation of centre of gravity locations are dependent on the manner in which the aircraft is loaded in terms of passengers, cargo and fuel.

The loading diagram is computed by starting with the Operational Empty Mass (OEM) and the corresponding centre of gravity location. These values are determined in the *@Class2WeightEstimation* which is run prior to this module. With the centre of gravity location and OEM known, the aircraft is loaded. The loading process is started with the passengers, which have been split into three separate classes, economy, business, and first class leading to three different ellipses in Figure 3.3. These passengers are loaded either front-to-back or back-to front, leading to the most extreme forward and aft centre of gravity positions due to passengers respectively. Following the passengers, the cargo is loaded. No distinction is made in terms of classes for cargo, leading to only one shape. The cargo is also loaded either front-to-back or back-to-front, with similar respective extreme forward and aft centre of gravity locations. Finally, the fuel can only be loaded following

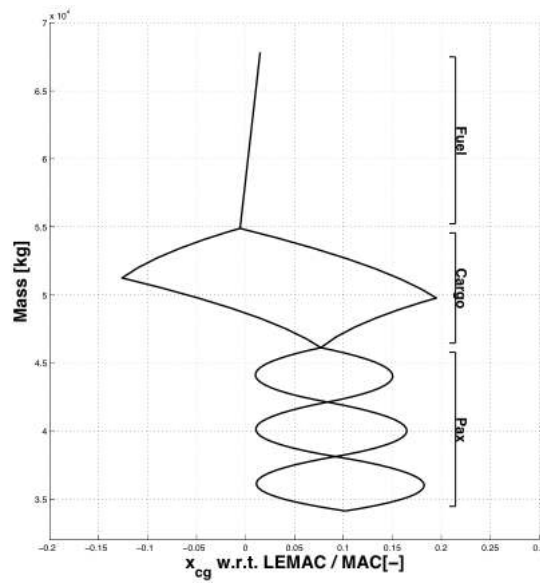


Figure 3.3: Example Loading Diagram [6]

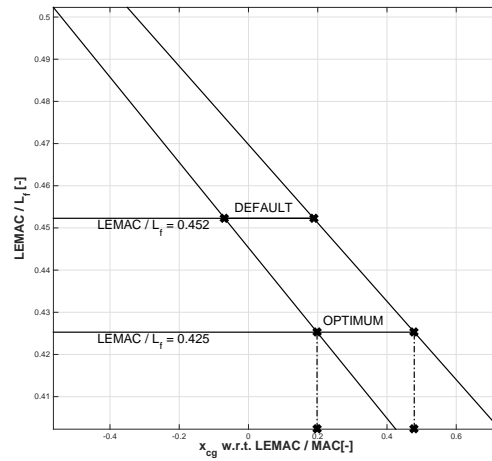


Figure 3.4: Example Centre of Gravity Ranges Diagram [6]

one scheme, and as such the centre of gravity position due to the fuel is shown as the final linear curve. Using this loading diagram, the most extreme forward and aft centre of gravity positions can be found.

The required horizontal tail area is dependent on the wing position. This is because a number of important variables, such as the centre of gravity of the operational empty aircraft and the aerodynamic centre, follow from this position. To find the minimum required horizontal tail area, this module runs the tail sizing method for a range of wing positions. This is done by finding the centre of gravity ranges using a loading diagram for three different wing positions, and interpolating between these three. This gives a centre of gravity ranges diagram as shown in Figure 3.4. The middle of the three wing positions is the default wing position, which is located at 45% of the fuselage length. The most forward and aft wing positions are located at 5% of the fuselage length ahead and behind the default wing position respectively.

3.3.2. X-PLOT METHODOLOGY

For a given wing position and centre of gravity location, the minimum horizontal tail area can be found using an x-plot. An x-plot, an example of which is shown in Figure 3.5, relates various forward and aft centre of gravity limits to the horizontal tail area. These limits were previously discussed in Section 2.3, however two

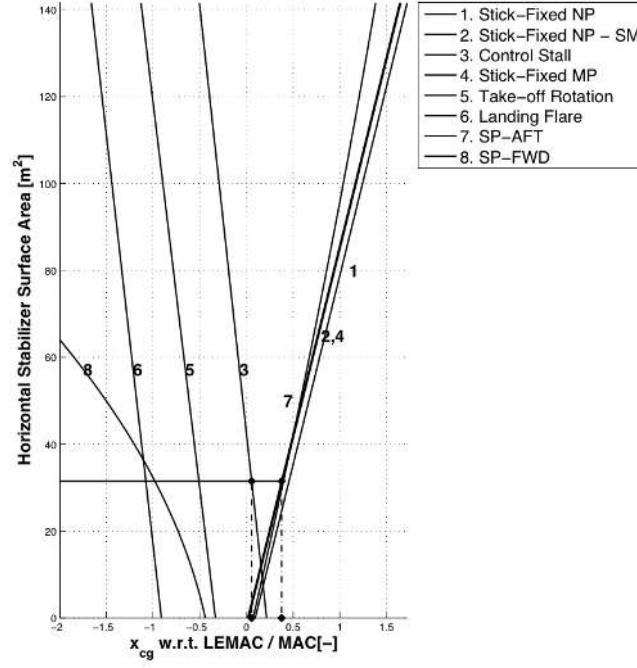


Figure 3.5: Example X-plot [6]

limits will be explained further in this section. These limits will be discussed as it gives a clear understanding of the working principle of the x-plot methodology as well as the fact that these limits will be used in further analysis of the propeller slipstream effect.

The first limit, which relates the aft center of gravity location to the horizontal tail area is the stick-fixed stability curve. As mentioned in Section 2.3, the stick-fixed stability curve indicates the horizontal tail area which is needed at a certain center of gravity position for a trimmed aircraft to provide a stabilizing pitching moment after a disturbance in angle of attack. This curve is shown in Figure 3.5 as curve 1. Mathematically, this curve is described according to Torenbeek [4] as:

$$\left(\frac{x_{cg}}{\bar{c}}\right)_{AFT} = \frac{x_{ac}}{\bar{c}} + \left[\frac{C_{L_{\alpha_h}}}{C_{L_{\alpha}}} \left(1 - \frac{d\varepsilon_h}{d\alpha}\right) \frac{s_h l_h}{s_w \bar{c}} \frac{V_h}{V_{\infty}} \right] \quad (3.7)$$

The implementation of propeller engines can have a significant influence on this relation by changing variables wing lift curve slope ($C_{L_{\alpha}}$), the downwash slope ($\frac{d\varepsilon_h}{d\alpha}$), and the flow velocity at the horizontal tail ($\frac{V_h}{V_{\infty}}$). The change in these variables due to propellers will be explained in Section 3.4.

The second limit follows from the takeoff rotation requirement mentioned in Section 2.3. This limit indicates the minimum horizontal tail area which is needed at a certain centre of gravity position for the aircraft to provide sufficient rotation for the aircraft to take-off. This curve is shown in Figure 3.5 as curve 5. Mathematically, this curve is described according to Torenbeek [4] as:

$$\left(\frac{x_{cg}}{\bar{c}}\right)_{FWD} = \left(\left[\left\{ \frac{s_h l_h}{S \bar{c}} - \frac{C_{L_R}}{C_{L_h}} \left(\frac{x_g}{\bar{c}} - 0.25 \right) \right\} \left(\frac{\eta_h \eta_q C_{L_h}}{C_{L_{max}}} \right) \right] - \frac{C_{m_{c/4}}}{C_{L_{max}}} \right) \frac{V_R^2}{V_S^2} \frac{x_g - z_T \Sigma T / W}{\bar{c}} \quad (3.8)$$

The implementation of propeller engines changes a large number of variables in this equation as will be explained in Section 3.4.

3.4. PROPELLER EFFECTS ON THE LONGITUDINAL STABILITY AND CONTROL

Part of the research objective as stated in the Introduction is to 'Develop and implement a prediction method for the propeller slipstream effect on the longitudinal stability and control in the conceptual design phase.

Following from the propeller slipstream explanation in Section 2.2, it can be understood that rotating propellers have a significant effect on many variables. This section aims to detail the implemented method used to determine the changes to the horizontal tail sizing variables.

The implemented method is based on Obert's method [10]. This method was chosen as it was the only readily available and computationally inexpensive method for the prediction of the propeller slipstream effect which lead to accurate results, as will be shown in Chapter 5. The method was slightly expanded to determine required variables which were not readily available during the Initiator design convergence. The additions to the method will be detailed in their corresponding subsections.

Following the same process as the method, this section will present the calculations used to determine the change in the most significant horizontal tail sizing variables. The variables to be examined are the propeller normal force(3.4.2), the tail-off lift coefficient(3.4.3), the tail-off pitching moment(3.4.4) and the tail-on pitching moment(3.4.5). First however, the most important assumptions which are made throughout this method are given.

3.4.1. ASSUMPTIONS

To develop a prediction method for the propeller slipstream effect that has acceptable runtimes during the conceptual design phase, assumptions have to be made. The main assumptions that are applicable throughout this method are:

- The slipstream rotation (swirl) and directional translation can be neglected
- No mixing occurs between the outer flow and the slipstream
- The slipstream cross-section remains circular with the contracted slipstream diameter at the horizontal tail
- For the determination of the tail-off lift coefficient, the axial velocity is considered to be uniform across the slipstream section

It should be noted that these assumptions and the implemented method are validated in Chapter 5. Despite this validation, further research should be done to reduce the number of assumptions made. This is discussed in the Recommendations in Chapter 7.

3.4.2. PROPELLER NORMAL FORCE

The direct influence of the propeller engines on the longitudinal stability and control is twofold. First is the direct contribution of the thrust to the lift due to the inclination of the engine with respect to the freestream flow. This contribution is the same for conventional jet or turbofan engines. However, it is still important to make note of this contribution as the thrust coefficient can differ significantly between propellers and jet engines for the same flight stage, as described in Section 2.1. The contribution can be described mathematically as:

$$C_{L_T} = C_T \sin \alpha \quad (3.9)$$

With:

$$C_T = \frac{T}{\frac{1}{2} \rho V^2 S} \quad (3.10)$$

The second influence, called the propeller normal force, is slightly more complex and occurs only for propeller engines. This force is best explained by describing a propeller engine with two propeller blades. With the propeller blades in the horizontal position, one can clearly denote an upward rotating blade and a downward rotating blade, as shown in Figure 3.6. When the propeller engine is at a positive angle of attack, the downward rotating blade experiences an increased loading in comparison to the upward rotating blade. This increase in loading is caused by an increased effective angle of attack and dynamic pressure of the downward rotating blade, compared to the upward rotating blade [8]. The increase in effective angle of attack and dynamic pressure is shown in the velocity diagrams in Figure 3.7. Both propeller blades cause a drag force, which is opposed in direction, as well as a lift force. However, as the downward rotating blade experiences the increased effective angle of attack it causes a larger drag force than the upward rotating blade. As a result,

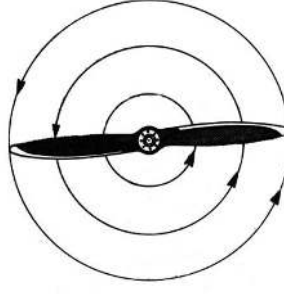


Figure 3.6: Propeller Blades Sketch [7]

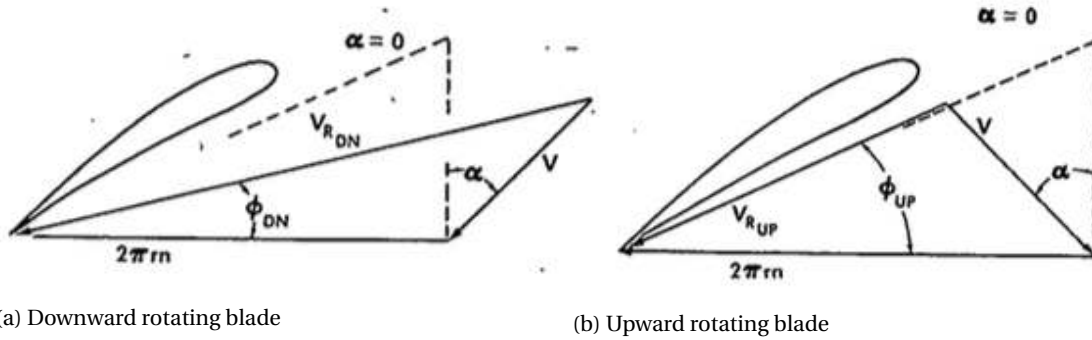


Figure 3.7: Velocity diagrams for a downward and upward rotating propeller blade section under an angle of attack [8]

a net upward drag is created called the propeller normal force.

In the 1940s, an evaluation method was developed by Ribner [23] based on strip theory which predicted the propeller normal force for small or moderate inclination angles [24]. In the mid-1960s, de Young [8] simplified this method and extended it to allow for higher angles of attack. The simple set of equations by de Young are used in ESDU packages [24] and have been implemented in this methodology.

The simple set of equations as derived by de Young [8] are as follows. The normal-force coefficient based on the freestream-velocity and propeller disk area differentiated with respect to the inflow angle at the propeller disk is computed with:

$$C'_{N_{\alpha_{in}}} = \frac{4.25\sigma_e}{1+2\sigma_e} \sin(\beta+8) \left(1 + \frac{3T'_c}{8\sqrt{1+\frac{2}{3}T'_c}} \right) \quad (3.11)$$

For single-rotation propellers and:

$$C'_{N_{\alpha_{in}}} = \frac{3.86\sigma_e}{1+\sigma_e} \sin(\beta+14) \left(1 + \frac{3T'_c}{8\sqrt{1+\frac{2}{3}T'_c}} \right) \quad (3.12)$$

For counter-rotating propellers. In these equations, the blade angle at .75 radius of the propeller blade (β) was assumed to be 26 degrees. This variable has been entered in the Initiator as a setting until propeller engines are completely sized in the Initiator which should give a blade angle depending on the flight condition. The effective propeller solidity (σ_e) is found using:

$$\sigma_e = \frac{\bar{b}'}{b'_{0.75}} \left(\frac{4B}{3\pi} \frac{b'_{0.75}}{D} \right) \quad (3.13)$$

Where the average blade chord (\bar{b}') is approximated with:

$$\frac{1}{0.8} \int_{0.2}^1 b' dr' = 0.16 \left(\frac{5}{4} b'_{0.25} + 2b'_{0.50} + 2b'_{0.75} + b'_{0.95} \right) \quad (3.14)$$

In this equation, the blade chords at various stations along the propeller blade were set to values found for a Dowty Rotol six bladed propeller used on the Fokker 50 [25]. These chords have been implemented as settings in the Initiator. Should a module be developed to accurately size the propeller blade geometry within the Initiator at a later date, these settings can easily be changed. The inflow angle at the propeller disk which is needed to complete the calculation for the propeller normal force can be equated using:

$$\alpha_{prop} = \frac{d\alpha_{in}}{d\alpha} (\alpha_r - \alpha_{C_L=0}) + \alpha_{C_L=0} + i_{prop} \quad (3.15)$$

Where the local angle of attack gradient is determined using:

$$\frac{d\alpha_{in}}{d\alpha} = 1 + \frac{2A_W}{9(A_W + 10)} \left(\frac{\frac{1}{X_{L,75}}}{c_r} \frac{1}{10} + \frac{\frac{1}{X_{R,75}}}{c_r} \frac{1}{10} \right) + \frac{1}{2} \left[\left(\frac{R_{fus}}{Y_{L,75}} \right)^2 + \left(\frac{R_{fus}}{Y_{R,75}} \right)^2 \right] \quad (3.16)$$

Finally, the propeller normal force is found using:

$$C_{Lp} = C'_{N_{\alpha_{in}}} \left[\frac{d\alpha_{in}}{d\alpha} (\alpha_r - \alpha_{C_L,0}) + \alpha_{C_L,0} + i_{prop} \right] \frac{\eta_e \frac{\pi}{4} D_{prop}^2}{S_W} \frac{1}{57.3} \quad (3.17)$$

3.4.3. TAIL-OFF LIFT COEFFICIENT

The propeller slipstream has two major effects on the lift over a wing. First, the dynamic pressure over the surface of the wing coinciding with the slipstream increases due to the increased flow velocity behind the propeller, as described in Section 2.2. Secondly, the effective angle of attack over the same surface changes as the airflow is deflected behind the propeller. To determine the change in lift over the wing due to the propeller slipstream, a method developed by Stepniewsky [26] which incorporates lifting line theory was used. According to lifting line theory, the lift on a wing can be determined using [10]:

$$L_W = \dot{m}_0 V_0 \sin \varepsilon = \rho \frac{\pi}{4} b_W^2 V_0^2 \sin \varepsilon \quad (3.18)$$

This equation states that the flow can be considered as a stream tube with circular cross section and diameter equal to the span of the wing which is deflected over the downwash angle (ε). Stepniewsky expanded on this by stating that the lift due to propeller slipstream is equal to the momentum resulting from the downward deflection of each streamtube of the propeller slipstream deflected over the slipstream downwash angle (ε_s) [26]. Mathematically, this gives the following equation:

$$L_S = n_e \dot{m}_s (V_0 + \Delta V) \sin \varepsilon_s = n_e \rho \frac{\pi}{4} D^{*2} (V_0 + \Delta V)^2 \sin \varepsilon_s \quad (3.19)$$

In this equation, (D^*) is the contracted slipstream diameter is the result of the contraction mentioned in Section 2.2.2. The contracted slipstream diameter is dependent on the propeller diameter, freestream flow velocity and velocity increase over the propeller blade as given by Roskam [2]:

$$D^* = D \sqrt{\frac{V_0 + \Delta V/2}{V_0 + \Delta V}} \quad (3.20)$$

Furthermore, the velocity increase in the fully contracted slipstream (ΔV) can be calculated using Equation 3.21 which was first given in Section 2.1:

$$\frac{(V_e - V_0)}{V_0} = \sqrt{1 + C_T \frac{S}{n_e A}} - 1 \quad (3.21)$$

Where:

$$\Delta V = V_e - V_0 \quad (3.22)$$

To calculate the lift over a wing with slipstream present, the total cross-sectional area of the contracted slipstream tubes need to be subtracted from the cross-sectional area describing the outer flow. Doing so gives the lift over a wing with a propeller slipstream present:

$$L_{W+S} = \rho V_0^2 \left[\frac{\pi}{4} b_W^2 - n_e \frac{\pi}{4} D^{*2} \right] \sin \varepsilon + \rho [V_0 + \Delta V]^2 n_e \frac{\pi}{4} D^{*2} \sin \varepsilon_s \quad (3.23)$$

$$C_{L_{W+S}} = \frac{L_{W+S}}{\frac{1}{2} \rho V_0^2 S_W} = \frac{2}{S_W} \left(\frac{\pi}{4} b_W^2 - n_e \frac{\pi}{4} D^{*2} \right) \sin \varepsilon + n_e \frac{\pi D^{*2}}{2 S_W} \frac{(V_0 + \Delta V)^2}{V_0^2} \sin \varepsilon_s \quad (3.24)$$

The downwash due to slipstream (ε_s) is estimated by again using the assumption that the lift due to slipstream is equal to the lift on a wing in free flow with a span equal to the diameter of the fully contracted slipstream and an airfoil section equal to the wing section at the propeller axes with flaps deflected [10]. Combining this assumption with lifting line theory gives:

$$\sin \varepsilon_s = \frac{2 C_{L_{\alpha_s, \text{eff}}}}{\pi A_{S, \text{eff}}} \sin \alpha_s \quad (3.25)$$

The effective aspect ratio of the wing part immersed in the slipstream ($A_{S, \text{eff}}$) is dependent on the thrust coefficient. It is computed using:

$$A_{S, \text{eff}} = A_S + (A_W - A_S) \left(\frac{V_0}{V_0 + \Delta V} \right)^{(A_W - A_S)} \quad (3.26)$$

The effective lift-curve slope of the slipstream section of the wing ($C_{L_{\alpha_s, \text{eff}}}$) is found using Figure 3.8. This figure was originally given in NACA report 1098 [9] but digitized and implemented in the Initiator. The angle of attack of this section (α_s) is the angle between the effective propeller slipstream centre line and the zero-lift angle of attack with flaps deflected. Mathematically this is described as:

$$\alpha_s = \alpha^* + i_{c_s} - \alpha_0 - \Delta \alpha_{0, f} \quad (3.27)$$

Where (i_{c_s}) is the angle of incidence of the local wing chord with respect to the fuselage reference line, (α_0) is the zero-lift angle of attack of the relevant airfoil section and ($\Delta \alpha_{0, f}$) is the change in zero-lift angle of attack due to flap deflection. Finally, the change in flow direction due to the acceleration of the flow at the propeller disk (α^*) is calculated using:

$$\alpha^* = \arctan \frac{V_0 \sin \alpha_R}{V_0 \cos \alpha_R + \Delta V / 2} \quad (3.28)$$

The downwash directly behind the wing without propeller slipstream (ε), which was required to calculate the lift of the wing and slipstream ($C_{L_{W+S}}$), was found using lifting line theory:

$$\sin \varepsilon = \frac{2 C_{L_{P-O}}}{\pi A_W} \quad (3.29)$$

In this equation, the power-off lift coefficient was found by modeling the wing in @AVL VLM [27]. This is in contrast with the calculations by Obert which use wind tunnel results for the power-off lift coefficient for the calculations. The tail-off power-off lift coefficient calculated using this method is validated in the results in Chapter 5.

At this point it is useful to make note of the the original downwash prediction method implemented by Quinten Jansen [6]. The method also uses AVL. However, for the downwash the tail and wing are modeled. In this model the incidence angle of the horizontal tailplane is varied iteratively until the lift coefficient of the tail reaches zero. This incidence angle is then added to the aircraft angle of attack to find the downwash due to the wing without rotating propellers as shown below:

$$\varepsilon = \alpha_R + i_h |_{C_{L_h}=0} \quad (3.30)$$

This downwash prediction method is presented in detail in the thesis of Jansen [6]. Some improvements were made to this method to improve its flexibility. These changes are presented in Section 4.1. The downwash calculated using this method will be used further in the calculation of the tail-on pitching moment in Section 3.4.5

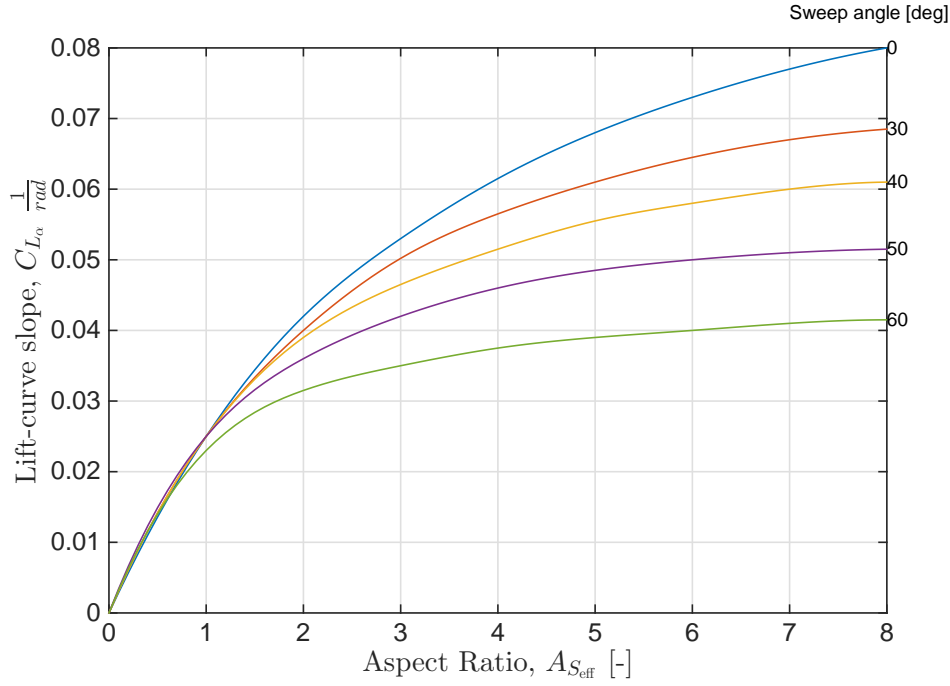


Figure 3.8: Variation of lift-curve slope with aspect ratio, taper ratio, and sweepback for subsonic incompressible flow [9]

With all these contributions to the tail-off lift coefficient known. The total tail-off lift coefficient can be determined as:

$$C_{L_{T-O}} = C_{L_{W+S}} + C_{L_P} + C_{L_T} \quad (3.31)$$

Using this, the lift purely due to propeller slipstream can be calculated using:

$$\Delta C_{L_S} = C_{L_{T-O}} - C_{L_{P-O}} - C_{L_T} - C_{L_P} \quad (3.32)$$

3.4.4. TAIL-OFF PITCHING MOMENT

The change in tail-off pitching moment due to rotating propellers results mainly from the change in three variables. These are the increased flow velocity in the propeller slipstream and the resulting increased tail-off lift coefficient described in the previous section, the propeller normal force described in Section 3.4.2 and the thrust. To determine the pitching moment, an illustration of the entire aircraft is given in Figure 3.9. The reference frame used in this figure will be used for the following discussion. For clarification, the three contributions to the tail-off pitching moment and the power-off tail-off pitching moment are shown in Figure 3.10. Following from this figure, the tail-off pitching moment in the power-on condition about the quarter chord point of the mean aerodynamic chord can be calculated as:

$$[C_{m_{\bar{c}/4}}]_{T-O} = C_{m_{P-O}} + C_{m_S} + C_{m_T} + C_{m_P} = C_{m_{P-O}} + [C_{m_{\bar{c}/4}}]_{\text{Prop}} \quad (3.33)$$

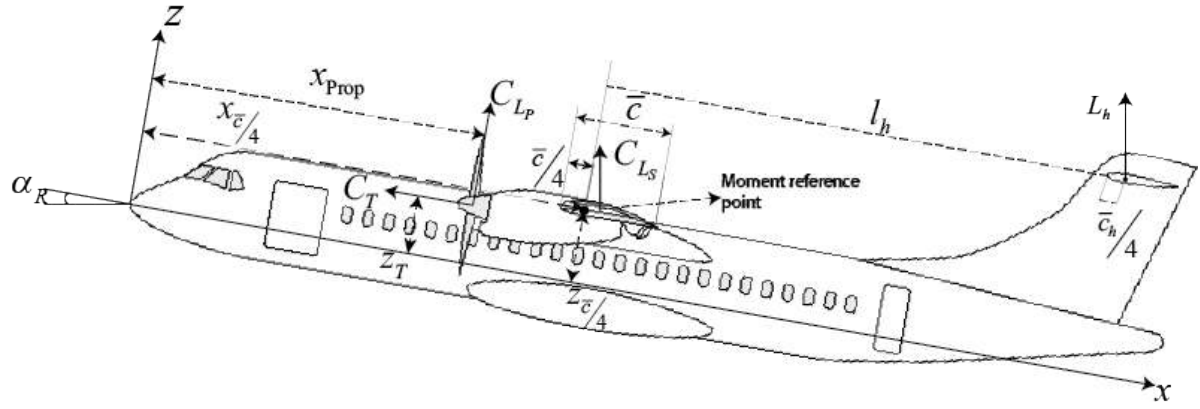


Figure 3.9: Illustration of the change in pitching moment due to propeller engines

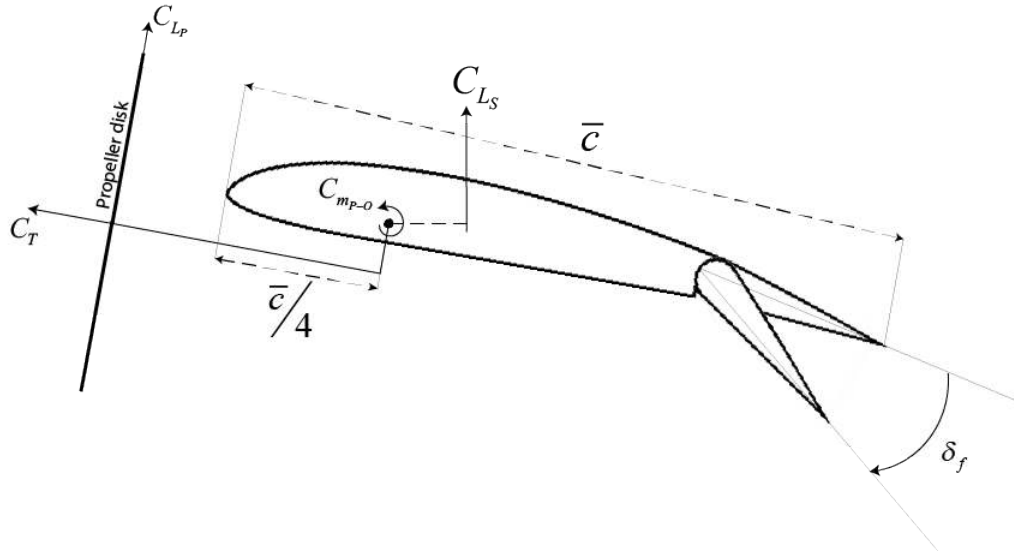


Figure 3.10: Contributions to the tail-off pitching moment due to propeller engines

The three contributions to the pitching moment will be discussed. The first contribution to be discussed is also the most complex. It is caused by the change in flow velocity over the wing in the propeller slipstream (C_{m_s}). Starting with a clean wing, the contribution to the pitching moment of the propeller slipstream can be computed as:

$$C_{m_{s,0}} = n_e \frac{D^* c_s}{S_W} C_{m_{0,s}} \left[\left(\frac{V_0 + \Delta V}{V_0} \right)^2 - 1 \right] \quad (3.34)$$

In this equation, the -1 has been included to ensure this increase is only due to the increased flow velocity in the slipstream, rather than also the outer flow. This was added as an addendum to the original report by Obert in [28]. For clean wings, the increase in lift due to propeller slipstream is assumed to apply at the quarter-chord point of the chord at the propeller axis. When flaps are deflected, this no longer holds true as the change in lift coefficient is applied to the extended chord. According to Glauert [29], the potential flow solution for the change in pitching moment due to increased lift over a wing with extended flaps is:

$$\left[\frac{dC_{m_{\bar{c}/4}}}{dC_L} \right] = \frac{c'}{c} \left[-0.25 + 0.32 \frac{c_f}{c'} \right] \quad (3.35)$$

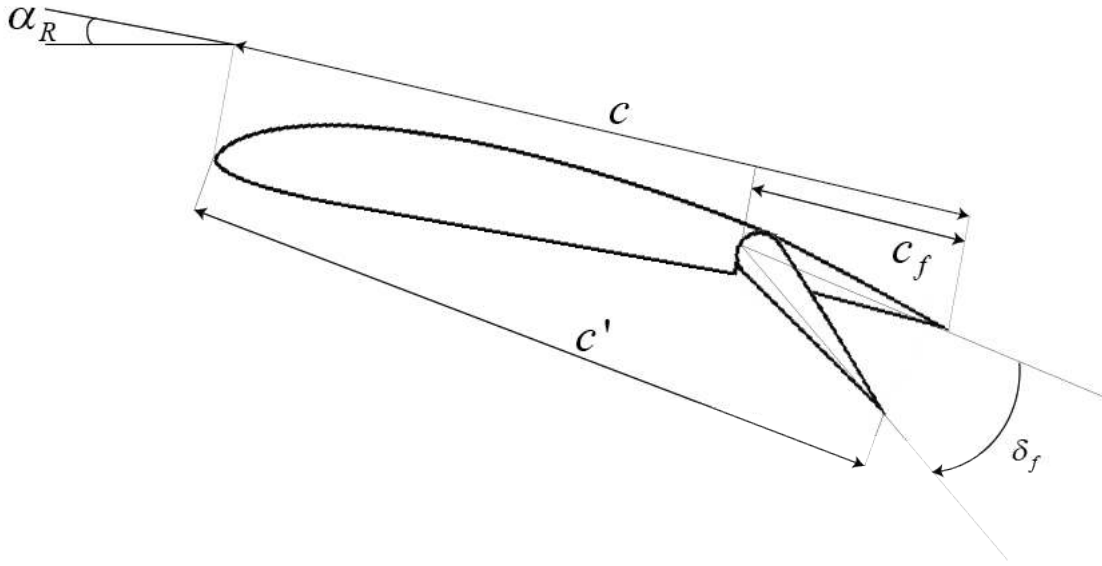


Figure 3.11: Chord definitions

In this equation, the wing section chord (c), the flap chord (c_f) and the extended chord (c') are defined as shown in Figure 3.11. This equation states that, the pitching moment taken about the quarter-chord point becomes more negative when flaps are deflected. This is due to the fact that the point of application of the increased lift over the flaps is further back, resulting in a larger moment arm and thus a larger negative moment. By examining numerous windtunnel test results, good correlation was found by expanding the equation [10] to:

$$\left[\frac{dC_{m_{\bar{c}/4}}}{dC_{L_{S,0}}} \right] = \frac{c'}{c} \left[-0.25 + 0.32 \frac{c_f}{c'} \right] \left[1 + 0.2 \left(1 - \sqrt{2} \sin \delta_f \right) \right] \quad (3.36)$$

To distinguish between flap effects and angle of attack effects, the lift coefficient at the zero-lift angle of attack due to slipstream ($\Delta C_{L_{S,0}}$) is applied to this expression. The change in pitching moment about the quarter-chord point of the extended chord due to lift caused by the propeller slipstream at angle of attack ($\Delta C_{L_{S,\alpha}}$) is determined using:

$$\left[\frac{dC_{m_{\bar{c}/4}}}{dC_{L_{S,\alpha}}} \right] = -0.25 \left[\frac{c'}{c} - 1 \right] \Delta C_{L_{S,\alpha}} \quad (3.37)$$

Adding these three expressions together gives the total change in pitching moment due to propeller slipstream over a wing with flaps deflected:

$$C_{m_S} = n_e \frac{D^* c_s}{S_W} C_{m_{0,s}} \left[\left(\frac{V_0 + \Delta V}{V_0} \right)^2 - 1 \right] + \frac{c'}{c} \left[-0.25 + 0.32 \frac{c_f}{c'} \right] \left[1 + 0.2 \left(1 - \sqrt{2} \sin \delta_f \right) \right] \Delta C_{L_{S,0}} - 0.25 \left[\frac{c'}{c} - 1 \right] \Delta C_{L_{S,\alpha}} \quad (3.38)$$

With this contribution to the pitching moment due to rotating propellers known, the remaining propeller normal force and thrust contributions need to be calculated. The contribution due to the propeller normal force is found by multiplying the propeller force, with the distance between the centre of gravity of the aircraft and the propeller disk as shown below:

$$C_{m_P} = - \frac{X_{CG} - X_{prop}}{c} \times C_{L_P} \quad (3.39)$$

The pitching moment contribution due to the propeller thrust can similarly be calculated using:

$$C_{m_T} = - \frac{Z_T - Z_{CG}}{c} \times C_T \quad (3.40)$$

Adding these three contributions together gives the change in tail-off pitching moment due to rotating propellers as:

$$[C_{m_{\bar{c}/4}}]_{\text{Prop}} = n_e \frac{D^* C_S}{S_W} C_{M_{0,S}} \left[\left(\frac{V_0 + \Delta V}{V_0} \right)^2 - 1 \right] + \frac{c'}{c} \left[-0.25 + 0.32 \frac{c_f}{c'} \right] \times [1 + 0.2(1 - \sqrt{2} \sin \delta_f)] \Delta C_{L_{S,0}} - 0.25 \left[\frac{c'}{c} - 1 \right] \Delta C_{L_{S,\alpha}} - \frac{X_{CG} - X_{prop}}{\bar{c}} \times C_{L_P} - \frac{Z_T - Z_{CG}}{\bar{c}} \times C_T \quad (3.41)$$

However, when comparing this equation to windtunnel test results, Obert discovered that the results were slightly offset [10]. Through correlation of the test results with the pitching moment equation so far, an additional shift to the point of application of the total wing lift due to the slipstream was added. This shift was added to allow for a better agreement with test data and as a result is of an empirical nature. The shift (ΔX_S), was originally calculated at higher flap angles. At these high flap angles it was approximated as:

$$\Delta C_{m_S} = -\frac{\Delta X_S}{c} \times \Delta C_{L_{S,\alpha}} = -\left[0.05 + 0.5 \left(\frac{c'}{c} - 1 \right) \right] \Delta C_{L_{S,\alpha}} \quad (3.42)$$

As the approximation above was computed with large flap deflections ($\delta_f \geq 30 \text{ deg}$), it was later found to not hold up with flaps retracted [28]. In the flaps retracted situation, the effect of propeller slipstream on upwash at the forward fuselage and engine nacelles still occurs however. The influence of this upwash on the pitching moment is determined using:

$$\Delta C_{m_S} = -\frac{\Delta X_{AC_{\text{fus}}}}{c} \times \Delta C_{L_{S,\alpha}} \quad (3.43)$$

In this equation, the shift in point of application due to fuselage ($\Delta X_{AC_{\text{fus}}}$) was entered in the Initiator as a setting. The default value was set to -0.25 . To make the above equations more easily applicable, an arbitrary equation was implemented:

$$\Delta C_{m_S} = -\left[\frac{\Delta X_{AC_{\text{fus}}}}{c} + \left(\frac{\Delta X_S}{c} - \frac{\Delta X_{AC_{\text{fus}}}}{c} \right) \frac{\delta_f}{30} \right] \Delta C_{L_{S,\alpha}} \quad (3.44)$$

Finally, adding this equation to the previous three contributions gives the total tail-off pitching moment due to rotating propellers:

$$[C_{m_{\bar{c}/4}}]_{\text{Prop}} = n_e \frac{D^* C_S}{S_W} C_{M_{0,S}} \left[\left(\frac{V_0 + \Delta V}{V_0} \right)^2 - 1 \right] + \frac{c'}{c} \left[-0.25 + 0.32 \frac{c_f}{c'} \right] \times [1 + 0.2(1 - \sqrt{2} \sin \delta_f)] \Delta C_{L_{S,0}} - 0.25 \left[\frac{c'}{c} - 1 \right] \Delta C_{L_{S,\alpha}} - \frac{X_{CG} - X_{prop}}{\bar{c}} \times C_{L_P} - \frac{Z_T - Z_{CG}}{\bar{c}} \times C_T - \left[\frac{\Delta X_{AC_{\text{fus}}}}{c} + \left(-\left[0.05 + 0.5 \left(\frac{c'}{c} - 1 \right) \right] - \frac{\Delta X_{AC_{\text{fus}}}}{c} \right) \frac{\delta_f}{30} \right] \Delta C_{L_{S,\alpha}} \quad (3.45)$$

It should be noted that this equation is only valid if the moment reference centre is taken about the quarter chord point of the mean aerodynamic chord. If not, an additional component needs to be added:

$$\Delta C_{m_S} = \frac{X_{CG} - X_{\bar{c}/4}}{\bar{c}} \times \Delta C_{L_S} \quad (3.46)$$

Finally, these calculations all lead to the total tail-off pitching moment equation at the beginning of this section:

$$[C_{m_{\bar{c}/4}}]_{T-O} = C_{m_{P-O}} + [C_{m_{\bar{c}/4}}]_{\text{Prop}} \quad (3.47)$$

3.4.5. TAIL-ON PITCHING MOMENT

The total tail-on pitching moment (C_m) is calculated by adding the horizontal tail pitching moment (ΔC_{m_h}) to the previously calculated tail-off pitching moment, or simply:

$$C_m = C_{m_{T-O}} + \Delta C_{m_h} \quad (3.48)$$

Where the horizontal tail pitching moment is equated using:

$$\Delta C_{m_h} = -C_{L_{\alpha,h}} \bar{V}_h (\alpha_r - \varepsilon + i_h) \frac{q_h}{q} \quad (3.49)$$

This equation contains three variables which are not immediately available as an input in the Initiator. These are the lift curve slope of the horizontal tail ($C_{L_{\alpha,h}}$), the total downwash angle at the tail (ε), and the dynamic pressure at the tail (q_h). This section will describe the method used for each variable.

LIFT CURVE SLOPE OF THE HORIZONTAL TAIL

The lift curve slope of the horizontal tail is determined using two @AVLVM runs with just the horizontal tail surface under two different angles of attack. By doing so, no downwash from the wing affects the lift curve slope of the tail. The default airfoil chosen for the tail is the N0012 airfoil [30]. However, this airfoil can be changed to improve the accuracy of the method as was done for the Saab 340 results, which used a NASA MS(1)-0312 airfoil [31] [30]. By using @AVLVM to compute the lift curve slope of the tail, the implemented method deviates again from the Obert's method as Obert uses estimates or wind tunnel results to find these variable which are not feasible for the Initiator.

VERTICAL DISTANCE SLIPSTREAM CENTRE LINE

Before explaining the methods used to determine the downwash and dynamic pressure, the vertical distance between the slipstream centre line and horizontal tail (h_{tot}) must be presented. This distance is required to calculate both values as will be described in their respective subsections.

The distance h_{tot} consists of four contributions which can be written as:

$$h_{\text{tot}} = h_t + \Delta h_e + \Delta h_l + \Delta h^* \quad (3.50)$$

These contributions are:

- h_t - The geometrical distance between the tail surface and the propeller axis at zero angle of attack
- Δh_l - The vertical displacement of the horizontal tail due to angle of attack
- Δh_e - The vertical displacement of the slipstream centre line passing through the clean wing's trailing edge
- Δh^* - The vertical displacement of the slipstream centre line due to the propeller axis not coinciding with the streamline leading to the forward stagnation point

The first contribution h_t is relatively easy as it can be determined immediately from the difference in the vertical position between the tail surface and the propeller axis:

$$h_t = Z_h - Z_{\text{prop}} \quad (3.51)$$

The second contribution Δh_l follows from the moment arm of the tail (l_h) with respect to the previously mentioned moment reference point, and the angle of attack as follows:

$$\Delta h_l = -l_h \times \sin \alpha_R \quad (3.52)$$

For the third contribution, Δh_e Obert [10] found that the slipstream centre line curves further downward behind the wing than the downwash behind the wing. This is illustrated in Figure 3.12. To calculate this vertical displacement, the so-called downwash factor ($K_e = Z_w / Z_e$) as noted in Figure 3.12 was found by Obert [10] based on the wind tunnel analysis of a single wing. The assumption was made that this downwash factor is valid for straight wings with an aspect ratio between 5 and 14. However, an additional study should be performed to check this assumption. The downwash factor K_e was determined based on the horizontal distance between the wing trailing edge and the tail (l^*) divided by the mean aerodynamic chord. The curve, shown in Figure 3.13 was implemented in the Initiator. Using this factor, the third contribution Δh_e was calculated as follows:

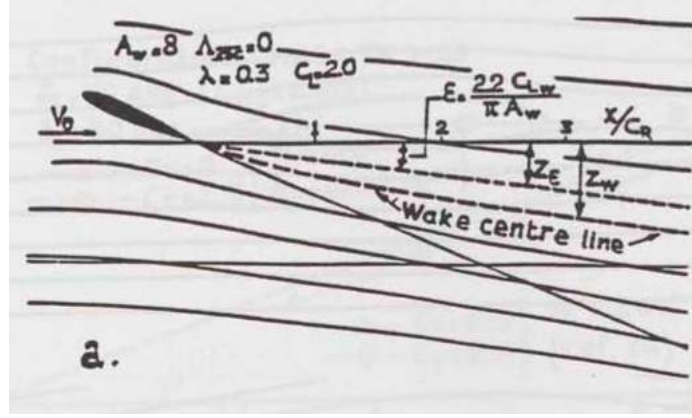


Figure 3.12: Sketch of the slipstream centre line behind the wing trailing edge [10]

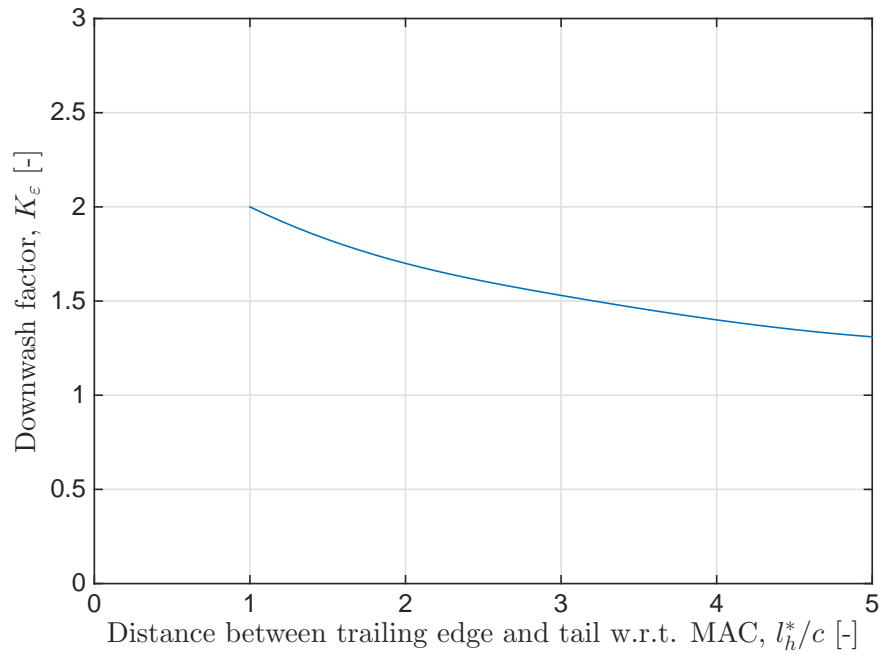


Figure 3.13: Downwash factor K_ϵ versus distance behind the wing trailing edge [10]

$$\Delta h_l = l_h^* \times \sin(K_\epsilon \times \epsilon) \quad (3.53)$$

In this equation, the downwash (ϵ) is calculated assuming no inflow effects which will be described in the following subsection.

The final contribution, Δh^* , is itself the result of three distances. The first of these is the displacement of the propeller disk due to angle of attack with respect to the quarter chord reference point:

$$(\Delta h^*)_\alpha = -(x_{c/4} - x_{\text{prop}}) \quad (3.54)$$

The second displacement is due to the fact that the trailing edge is displaced downwards due to flap deflection, calculated using:

$$(\Delta h^*)_f = c_f \times \sin \delta_f \quad (3.55)$$

The final contribution is the vertical displacement of the slipstream centre line caused by upwash in front of the wing due to flap deflection, calculated using:

$$(\Delta h^*)_{\text{upwash}} = 0.25 [x_{\bar{c}/4} - x_{\text{prop}}] \sin \Delta \alpha_{0,f} \quad (3.56)$$

Where the variable $\Delta \alpha_{0,f}$ is the change in airfoil section zero-lift angle of attack due to flap deflection. Again, @AVLVM was used to determine this value rather than estimating or using wind tunnel test data. Furthermore, the 0.25 coefficient was chosen empirically by examining the streamline pattern of a number of airfoil configurations [10]. Rewriting the equation for the total vertical distance between the slipstream centre line and the horizontal tail by expanding the four contributions then gives:

$$h_{\text{tot}} = Z_h - Z_{\text{prop}} - l_h \times \sin \alpha + l_h^* \times \sin (K_\epsilon \times \epsilon) - (x_{\bar{c}/4} - x_{\text{prop}}) + c_f \times \sin \delta_f + 0.25 [x_{\bar{c}/4} - x_{\text{prop}}] \sin \Delta \alpha_{0,f} \quad (3.57)$$

DOWNWASH

The downwash behind a wing with rotating propellers is assumed to consist of three major components.

The first component is the power-off downwash resulting primarily from lift over the wing. The power-off downwash is found using the @AVLVM method previously mentioned in Section 3.4.3. This component can be described mathematically as:

$$\epsilon_{P-O} = (\epsilon_0)_{P-O} + \left(\frac{d\epsilon}{dC_L} \right) C_{L_{P-O}} \quad (3.58)$$

Here, the downwash at the zero-lift angle of attack $[(\epsilon_0)_{P-O}]$ is a result of the fact that although the total lift is zero, the flow behind the wing is not necessarily the same as the undisturbed flow. There are various reasons for why this may occur, such as a non-elliptical lift distribution over the wing which give local lift contributions adding up to a zero total lift. Furthermore, upwash from the fuselage or nacelles also has an effect on the flow.

The second component consists of the change in downwash due to increasing lift over the wing by propeller slipstream. It is important to note at this point, that the assumption is made that the cause for the increase in lift is irrelevant for the downwash. This means that for a constant increase in lift, whether due to propeller slipstream, or an increase in angle of attack, the downwash increases with the same amount. As a result, the increase in lift due to propeller slipstream needs only to be multiplied with $\left(\frac{\delta \epsilon}{\delta C_L} \right)$. This gives the second component:

$$\epsilon_S = \left(\frac{d\epsilon}{dC_L} \right) \Delta C_{L_S} \quad (3.59)$$

The third component only occurs when the distance between the horizontal tail and the slipstream centre line is less than 1.25 times the contracted slipstream diameter (D^*). As the horizontal tail moves closer to the slipstream centre line, an inflow occurs from the external flow into the slipstream. This inflow is illustrated in Figure 3.14. From this figure, one can see that the downwash increases or decreases depending on whether the tail is above or below the slipstream centre line respectively. Using windtunnel test results, Obert [10] demonstrated that the downwash due to inflow is dependent on the increase in flow velocity in the contracted slipstream over the freestream velocity $\left(\frac{\Delta V}{V_0} \right)$. This leads to:

$$\Delta \epsilon = (\Delta \epsilon)_{\frac{\Delta V}{V_0}=1} \times \frac{\Delta V}{V_0} \quad (3.60)$$

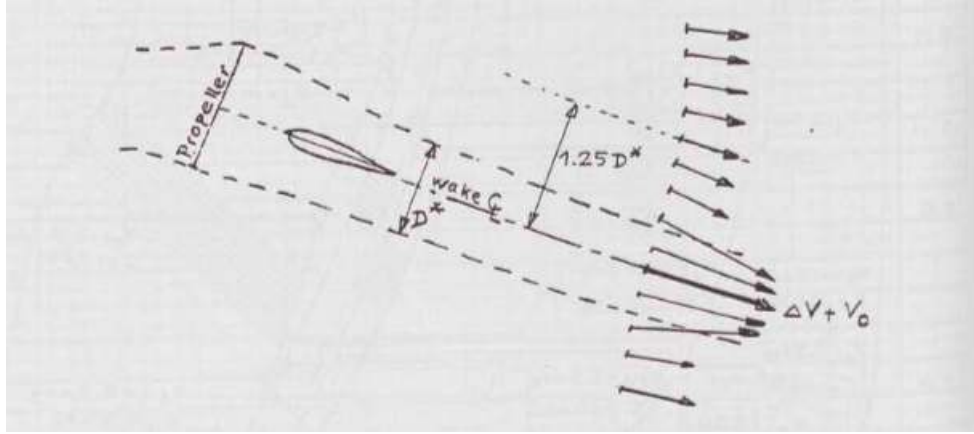


Figure 3.14: Schematic representation of the inflow effect of the external flow into the slipstream [10]

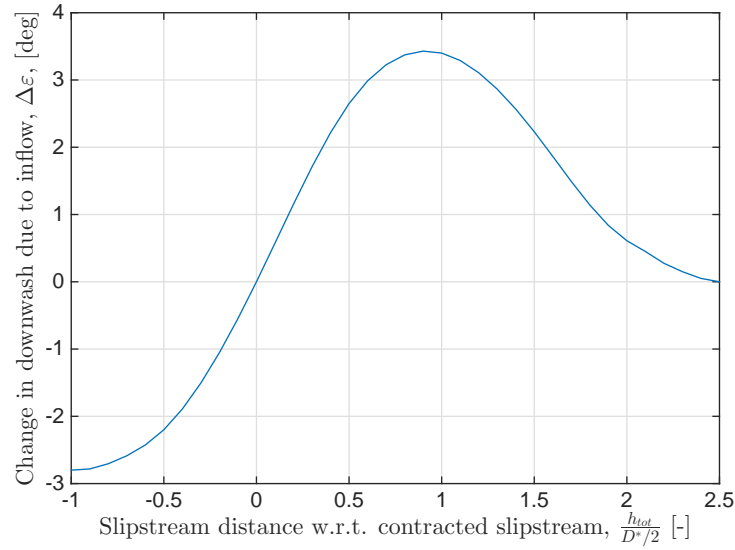


Figure 3.15: Change in downwash at the tailplane due to inflow into the slipstream - generalized curve

Using test data, the curve for $(\Delta\epsilon)_{\frac{\Delta V}{V_0}=1}$ was determined as a function of the previously mentioned distance between slipstream centre line and horizontal tail (h_{tot}). This curve is shown in Figure 3.15 [10].

Finally, combining the previously mentioned three components, the total average downwash with rotating propellers can be described using:

$$\epsilon = (\epsilon_0)_{P-O} + \left[\frac{d\epsilon}{dC_L} \right]_{P-O} \times [C_{L_{P-O}} + \Delta C_{L_S}] + (\Delta\epsilon)_{\frac{\Delta V}{V_0}=1} \times \frac{\Delta V}{V_0} \quad (3.61)$$

AVERAGE DYNAMIC PRESSURE

The average dynamic pressure at the horizontal tail (q_h) is determined by calculating how large the tail area covered by the propeller streamtubes is. This is done based on the assumptions in Section 3.4.1 and one additional assumption[10]:

- If four propeller engines are present, only the inner two streamtubes cover the tail.

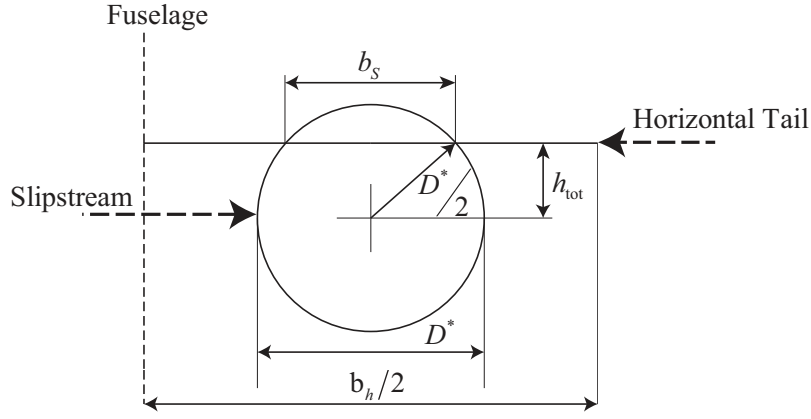


Figure 3.16: Tail span covered by the propeller slipstream

Using these assumptions, the tail area covered by the slipstream can be determined using the situation sketched in Figure 3.16. The tail area can be determined as:

$$S_s = 2 \times b_s \times c_{h_s} \quad (3.62)$$

Where the span of the tail covered by the slipstream is found using:

$$b_s = D^* \sqrt{1 - \left[\frac{h_{tot}}{D^*/2} \right]^2} \quad (3.63)$$

The average dynamic pressure at the tail can then be found using the assumption that no mixing occurs between the slipstream and outer flow. Using this assumption, the dynamic pressure is:

$$q_h = \frac{1}{2} \rho \left[1 + \frac{\Delta V}{V_0} \right]^2 V_0^2 S_s + V_0^2 [S_h - S_s] \quad (3.64)$$

Using the downwash and dynamic pressure as calculated, the tail-pitching moment can be calculated using the previously presented equation:

$$\Delta C_{m_h} = -C_{L_{\alpha,h}} \bar{V}_h (\alpha_r - \varepsilon + i_h) \frac{q_h}{q} \quad (3.65)$$

Which adds up to the total tail-on pitching moment:

$$C_m = C_{m_{T-O}} - C_{L_{\alpha,h}} \bar{V}_h (\alpha_r - \varepsilon + i_h) \frac{q_h}{q} \quad (3.66)$$

4

CODE IMPLEMENTATION

This chapter covers the way in which the methodology is to be implemented within the Initiator. The methodology has not been formally implemented in the Initiator for two reasons:

1. The overall propeller implementation has strong similarities to the work of van Bogaert [22] as we both worked on propeller implementation simultaneously. Both codes should be compared before implementation to ensure no overlap or inconsistencies occur.
2. The *@HorizontalStabilityEstimation* module is currently being corrected and reworked by another student. The propeller slipstream prediction method will be implemented into this module as soon as this work is done.

As a result, it is difficult to describe the exact implementation of the code within the Initiator at this time. Therefore, a short addendum will be written when the code is implemented to ensure future researchers can easily use it. However, at this time it is possible to list which files have been edited within a working copy of the Initiator as part of the propeller implementation and prediction methodology.

For the basic propeller implementation described in Section 3.2 no new MATLAB [32] files were added. Instead, existing files were expanded to include calculations based on turboprop engines. The engine type was simply checked in each file using:

```
switch EngineType
case 'TurboFan'
...
case 'TurboProp'
...
end
```

The MATLAB files that were expanded to include the basic propeller implementation are:

- @Class1WeightEstimation
 - propConstraints.m
- @GeometryEstimation
 - estimateEngines.m
 - positionEngines.m
- @Class2WeightEstimation
 - calculateReserveFuel.m
 - calculateTotals.m
 - getEngineWeight.m
 - getFuelWeight.m

- getSystemsWeight.m
- @EngineModel
 - run.m
- @AVLVLM
 - AVLVLm.m
 - createInput.m
 - runAVL.m
 - writeInput.m
 - run.m
- @ParasiteDragEstimation
 - engineDrag.m
- @MissionAnalysis
 - climbProp.m
 - cruiseProp.m
 - descentProp.m
 - emissionsProp.m
 - holdProp.m
 - landingProp.m
 - mission.m
 - rotationspeed.m
 - run.m
 - takeoffProp.m
- @PerformanceEstimation
 - run.m

As stated earlier, the changes made to these MATLAB files need to be compared with the code of van Bogaert [22] to ensure the same method is not implemented twice.

The code containing the propeller slipstream prediction method described in Section 3.4 is to be implemented in the *@HorizontalStabilityEstimation* module. This code will most likely be implemented within this module in two parts. The first part is a standalone file which carries out the calculations described in the methodology to determine the changes to the relevant longitudinal stability and control variables. The second part consists of editing existing files to change the relevant variables if propeller engines are used. This is done using the *switch* function described above. The files to be edited are:

- ControlStall.m
- DynamicStability.m
- FlowInterference.m
- GoAround.m
- InputVariables.m
- LandingFlare.m
- run.m
- StabilityNeutral.m
- TakeoffRotation.m
- xPlot.m

It should be reiterated that these changes are tentative and depend on the rework of the *@HorizontalStabilityEstimation* module.

4.1. MODULE IMPROVEMENTS

Having described the existing module as it was completed by Jansen in Section 3.3, it is important to note improvements which were already implemented as part of this thesis work. Once again, although these improvements were implemented, some errors remain within the module which another student is currently working on to resolve. The improvements mentioned here however have been completed.

The first and most important improvement was an overall rework of the vortex lattice method implementation within the module called *@AVLVLM* [27]. This rework involved two major changes. First was to change the program structure to have *@HorizontalStabilityEstimation* access the central *@AVLVLM* module, rather than using a simplified copy of the module. The second change regards the usage of flaps and slats in *@AVLVLM* computations. In the original work by Jansen, flaps and slats dimensions were hard coded in the module. As a result, variations in these dimensions were not easily altered during the design convergence. By making the flaps and slats parts within the *.xml* of the Initiator, *@AVLVLM* can automatically gather the dimensions from the *.xml* file. Currently, the dimensions of the flaps and slats are implemented as settings within the *settings.xml* file. However, should a module be developed at a later date to compute their dimensions, this can easily be changed.

The second improvement was to get rid of the large number of hard coded input variables within the code. These input variables, such as the ice accretion factor mentioned with the thesis of Jansen [6], have been coded as settings within the *settings.xml* file.

The final improvement has to do with general coding practices. The original module had a number of `while` loops which can cause the module to crash or remain in an infinite loop. These loops have been changed to `for` loops to make the module more robust.

5

RESULTS AND DISCUSSION

In this chapter, the results obtained by using the implemented methodology of the previous chapter are presented and discussed. These results serve two purposes. First, they validate the implemented method and show the accuracy of the method when compared to windtunnel test data. Secondly, they show the effect of the propeller slipstream effect on the horizontal tail sizing.

In this chapter, the results will be given first in Section 5.1 followed by a thorough discussion of these results in Section 5.2. Four types of results will be discussed, these will be ordered as follows. First, are the tail-off lift curves, which give the tail-off lift coefficient versus angle of attack in Subsection 5.1.1. The pitching moment curves, calculated using the method in Subsections 3.4.4 and 3.4.5, are given in Subsection 5.1.2. Both the tail-off lift curves and pitching moment curves include windtunnel test results to provide a validation of the methods as well as an indication of the propeller slipstream effect on these variables. Thirdly, the horizontal tail contribution versus angle of attack is shown in Subsection 5.1.3. These figures are used to give an indication of the change in tail effectiveness due to rotating propellers. Finally, Subsection 5.1.4 shows the effect of the propeller slipstream on the overall tail sizing using the x-plots under three flight conditions. The discussion in Section 5.2 will be structured in the same order.

Unfortunately, very little validation data exists for the propeller slipstream effect on the horizontal tail. The only useable data sets that could be found are for the Fokker 50 and Saab 340 aircraft [10] [28]. As a result, these are the only aircraft for which results are shown. However, the method can be applied to any aircraft which can be designed using the Initiator design loop. Sketches with dimensions for the Saab 340 and Fokker 50 are included in Appendix A

A special note has to be made for the results of the Saab 340 aircraft. This aircraft is relatively small and could not be accurately designed by the Initiator. To solve this, the dimensions for the Saab 340 were used as direct inputs for the method. Which means that any inconsistencies for this aircraft cannot be due to geometric differences between the Initiator design and the actual aircraft. Furthermore, the validation data for the Saab 340 is based on a special model with a T-tail configuration, allowing the effect of tail height to also be examined. The Fokker 50 was found using the Initiator design convergence and therefore validates the method within the entire Initiator as well as wing sizing resulting from the propeller implementation.

5.1. RESULTS

In this Section, the results are given accompanied by a brief explanation of the effects shown. A more critical interpretation of the results in terms of verification and analysis is presented in Section 5.2.

5.1.1. TAIL-OFF LIFT CURVES

The tail-off lift curves, which indicate the tail-off lift coefficient ($C_{L_{T-o}}$) versus angle of attack (α) at various propeller thrust coefficients and flap deflections, will be given per aircraft. The results for the Saab 340 will be given first, followed by the Fokker 50 results.

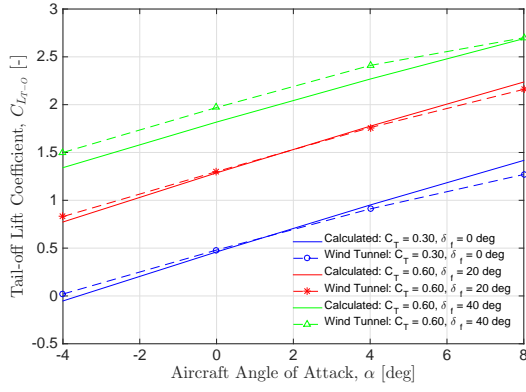


Figure 5.1: Tail-off lift curves - Saab 340

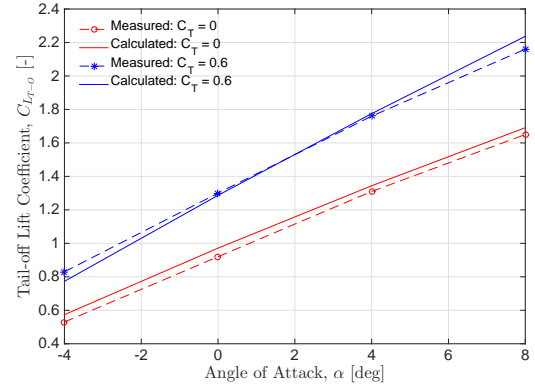


Figure 5.2: Tail-off lift curves - Saab 340 - Flaps 20 degrees

SAAB 340

As previously mentioned, the Saab 340 results were determined by entering direct geometric inputs into the method, foregoing the Initiator design convergence. The tail-off lift curves for the aircraft at various flap deflections and propeller thrust coefficients are shown in Figure 5.1. This figure shows a good comparison between the calculated values and the windtunnel test results which means the figure is very helpful in terms of validating the implemented method. However, it is difficult to discern the exact effect of the propeller slipstream on the tail-off lift coefficient from these curves as the flap deflection varies between curves as well. Nonetheless, it does seem as though an increase in thrust coefficient causes an increase in lift coefficient.

Figure 5.2 instead gives a clearer indication of the propeller slipstream effect on the lift curves. This figure shows the difference between the tail-off lift slopes in the power-off and power-on ($C_T = 0.6$) condition at a constant flap deflection of 20 degrees. As an example, at zero degrees angle of attack, the lift coefficient is increased by roughly 35%, proving the significance of the propeller slipstream. Furthermore, the figure again shows a good correlation between the measured and calculated results.

FOKKER 50

For the Fokker 50, more tail-off lift data was found, leading to more validation figures. Figures 5.3, 5.4, 5.5 and 5.6 contain the lift curves at a set flap deflection for increasing thrust coefficients. These figures again clearly show the increase in tail-off lift, due to propeller thrust as the lift curve slopes are steeper for higher thrust coefficients. Furthermore, as expected, the tail-off lift is higher at higher flap deflections.

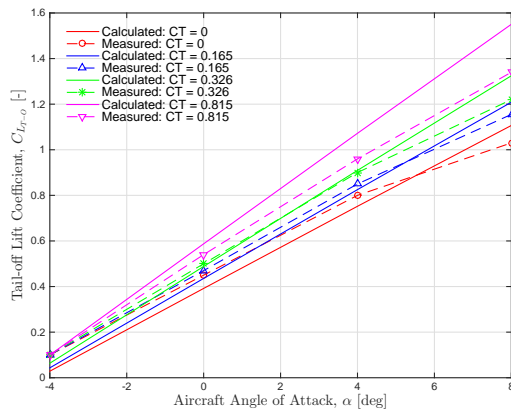


Figure 5.3: Tail-off lift curves - Fokker 50 - Flaps retracted

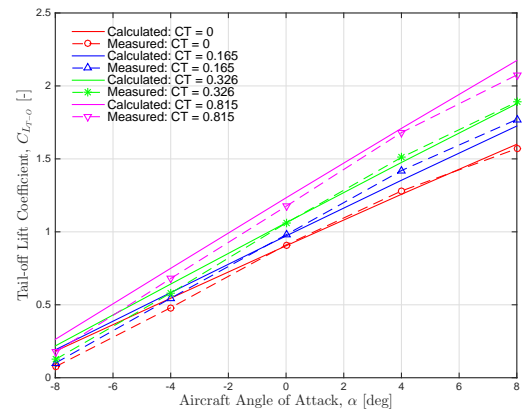


Figure 5.4: Tail-off lift curves - Fokker 50 - Flaps 16.5 degrees

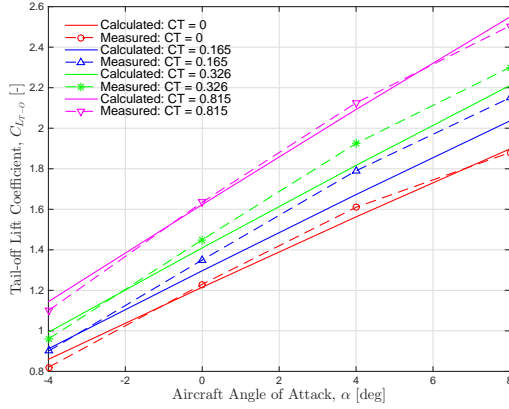


Figure 5.5: Tail-off lift curves - Fokker 50 - Flaps 26.5 degrees

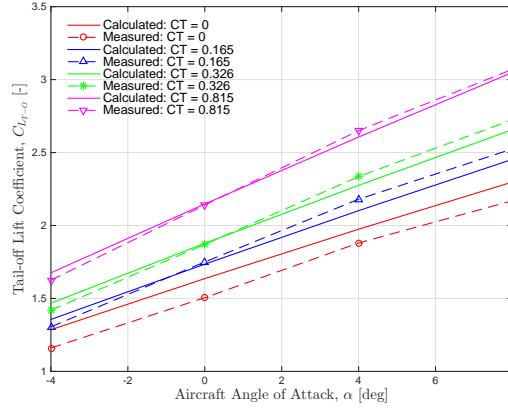


Figure 5.6: Tail-off lift curves - Fokker 50 - Flaps 40 degrees

5.1.2. PITCHING MOMENT CURVES

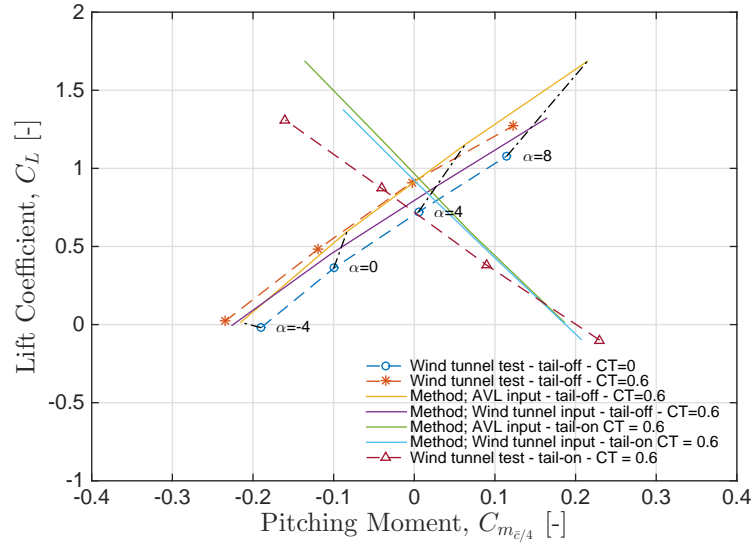
The pitching moment curves, indicating the tail-off and tail-on pitching moments about a certain reference point versus the corresponding lift coefficient, are given per aircraft. Again the Saab 340 results are presented first, followed by the Fokker 50. These figures were found by determining the lift coefficient and pitching moments at various angles of attack. As a result, constant angles of attack lines are also shown between the power-off and power-on lines to indicate the change in lift and pitching moment due to rotating propellers. It should be noted that the power-off tail-off moments were taken from the wind tunnel data, as the *@HorizontalStabilityEstimation* module does not correctly predict this yet. Work is being done to improve this by another student, however at the time of writing, this work was not completed yet.

SAAB 340

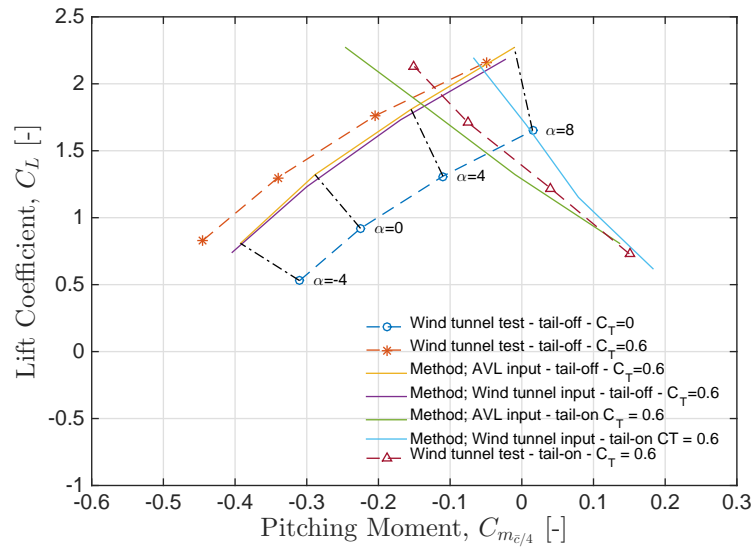
Three pitching moment figures are shown for the Saab 340 corresponding to three different flap settings, they are Figures 5.7a, 5.7b and 5.7c. It should be noted that the thrust coefficient for Figure 5.7a was 0.30, and for the other two figures was 0.60. These figures were made by computing the pitching moment about the quarter chord point of the mean aerodynamic chord and lift coefficients at various angles of attack using the method described in Section 3.4.4. They show both the tail-off and tail-on pitching moments according to three different sources. These are the windtunnel test results, the method with *@AVLVLM* input as implemented in the Initiator, and the method with windtunnel test inputs as calculated by Obert [28]. The reason for including the method with windtunnel test inputs was to give a clear indication for potential inconsistencies in results due to *@AVLVLM*. Finally, the wind tunnel test results for the power-off condition are shown to illustrate how propeller thrust affects the tail-off pitching moment. Unfortunately, no power-off tail-on pitching moment curves were tested.

The tail-off pitching moment curves show, especially when looking at the constant angle of attack lines, two major effects due to propeller thrust. The first is the increasing lift coefficient due to the propeller slipstream in the same manner as indicated in the previous section. The second is an overall decrease in pitching moment. This effect however reduces for higher angles of attack, and even becomes positive for the flaps retracted case, as will be explained in Section 5.2.

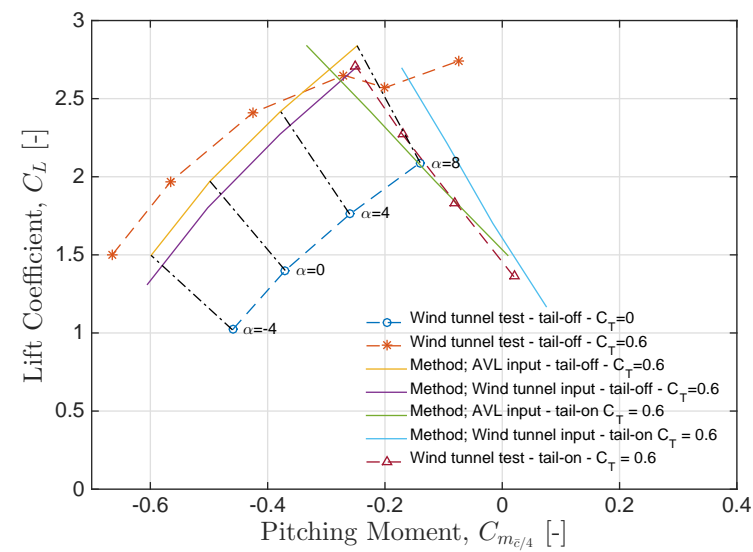
The tail-on pitching moment curves show that the pitching moment is positive at negative angles of attack, and becomes negative as the aircraft pitches upward as is expected. The tail-on curves here are shown primarily to validate the downwash prediction method described in Section 3.4.5.



(a) Flaps retracted

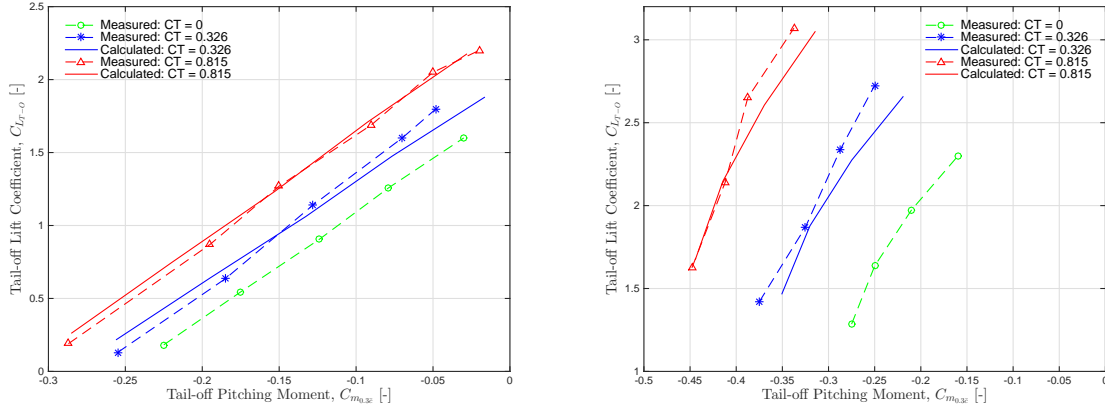


(b) Flap deflection = 20 degrees



(c) Flap deflection = 40 degrees

Figure 5.7: Pitching moment curves - Saab 340



(a) Flap deflection = 16.5 degrees

(b) Flap deflection = 40 degrees

Figure 5.8: Tail-off Pitching moment curves - Fokker 50

FOKKER 50

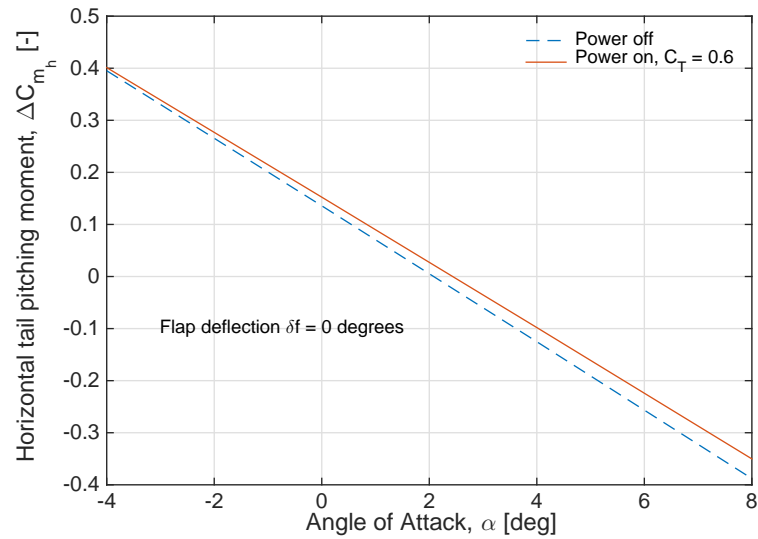
For the Fokker 50, the results found are shown in Figures 5.8a and 5.8b. These figures show the tail-off pitching moment curves at flap deflections of 16.5 degrees and 40 degrees. Unfortunately, no validation data was found for tail-on curves. The curves were computed in the same manner as for the Saab 340, in that the lift coefficients and pitching moment coefficients were computed at various angles of attack. Both figures show similar effects as the Saab 340. For increasing thrust coefficient, the tail-off lift coefficient increases as expected. The tail-off pitching moment also becomes more negative at higher thrust. Again, this effect lessens at higher angles of attack as will be explained in the discussion.

5.1.3. HORIZONTAL TAIL CONTRIBUTION

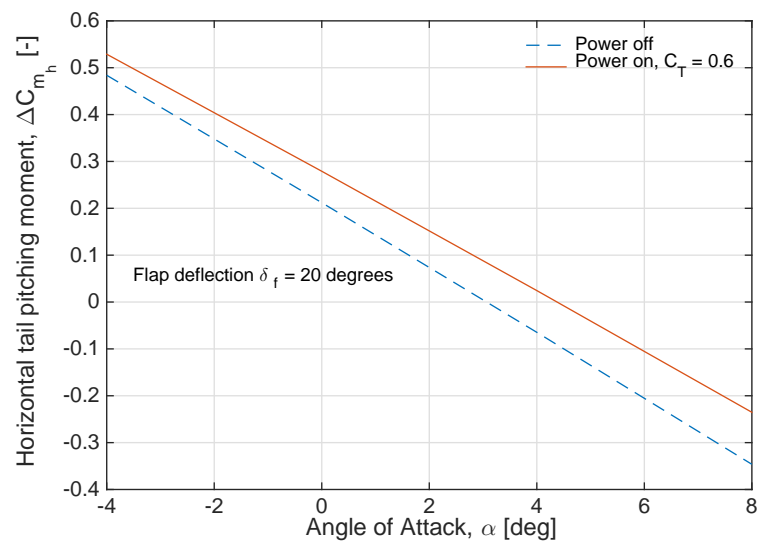
The horizontal tail pitching moment contribution (ΔC_{m_h}) versus angle of attack curves were calculated using the method described in Section 3.4.5. As explained in this section, the horizontal tail pitching moment is dependent on the downwash and average dynamic pressure at the tail. These variables are themselves dependent on the vertical distance between the horizontal tail and the slipstream centre line as described in the same section. As the Fokker 50 and Saab 340 differ in tail height, a significant difference was expected in tail pitching moment. This is confirmed by comparing the results given below.

SAAB 340

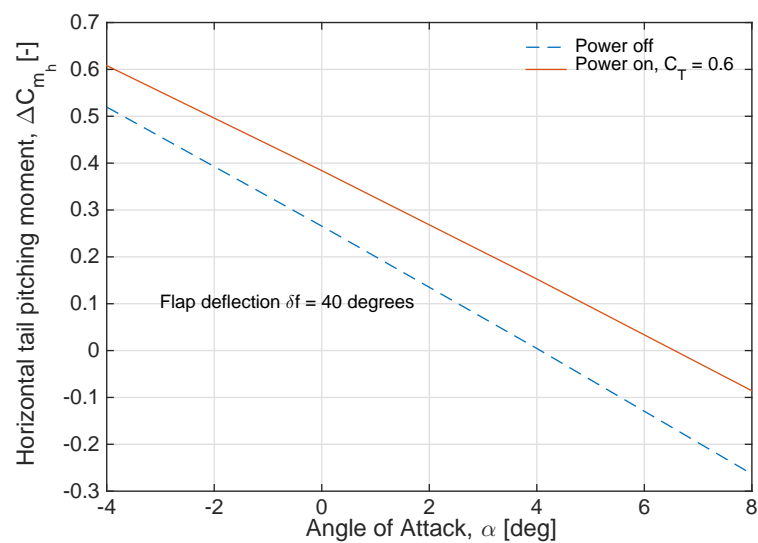
At this point it is important to reiterate the fact that the results for the Saab 340 are based on a special T-tail configuration used in wind tunnel tests. This leads to a large distance between the slipstream centre line and the horizontal tail. To analyze the effectiveness of the tail in this configuration, Figures 5.9a-5.9c show the effect of propeller slipstream in three different flap deflections. These figures show that the tail pitching moment follows a negative linear slope. Furthermore the difference between the power on and power off pitching moment contributions increases for higher flap deflections.



(a) Flaps retracted



(b) Flap deflection=20 degrees



(c) Flap deflection=40 degrees

Figure 5.9: Horizontal tail pitching moment - Saab 340

FOKKER 50

Unlike the special Saab 340 model, the Fokker 50 computations are based on the actual Fokker 50 configuration. This means that the aircraft has a low horizontal tail configuration. This low tail configuration leads to additional effects acting on the tail pitching moment as can be seen in Figures 5.10a - 5.11a. Similar to the Saab 340, these figures show the effect of propeller thrust on the tail pitching moment for three different flap deflections. Although the power off curves show a similar negative linear trend as before, the power on curves are drastically different. This difference occurs because of the nonlinear dynamic pressure and downwash inflow effects. Furthermore, this difference seems to depend on the flap deflection. These effects will be discussed in Section 5.2

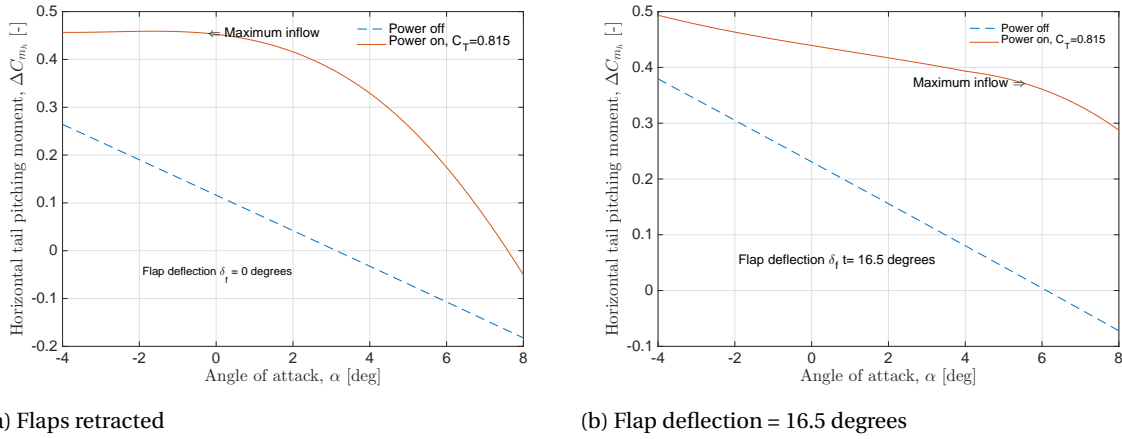


Figure 5.10: Horizontal tail pitching moment - Fokker 50

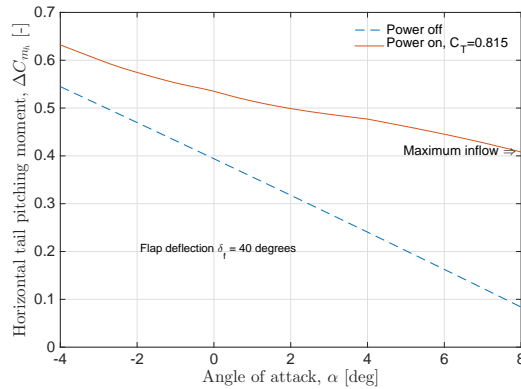


Figure 5.11: Horizontal tail pitching moment - Fokker 50

5.1.4. EFFECT ON TAIL SIZING

The effect on tail sizing can be examined using x-plots previously described in Section 3.3.2. As mentioned earlier, the `@HorizontalStabilityEstimation` module is not working currently. Therefore a temporary script was made to still perform this analysis. Unfortunately, this means that not all constraints are implemented and that the x-plots are only given for the default wing position. As a result, no actual tail sizing is examined. Instead, the shift in the three constraints due to propeller slipstream is examined. This means that no quantitative result can be given unfortunately. But a qualitative indication of the effect on tail sizing is possible.

The x-plots given here contain the stick-fixed stability, controllability required for stall, and control capacity required to rotate the aircraft during takeoff constraints. These constraints were presented in Section 3.3.2. As stated in that section, the assumption is made that the engines are idle for the landing condition used in

the control stall constraint. This means that only one curve is given for this constraint as the influence of propeller engines is irrelevant in this condition. The stick-fixed stability and takeoff rotation constraints are affected by propeller engines, and as such two curves are given for each constraint. In the same manner as the previous results, an x-plot will be given for each aircraft starting with the Saab 340.

SAAB 340

Figure 5.12 shows the x-plot based on the Saab 340 in the power-off and power-on condition. The figure shows that the stick-fixed stability constraint becomes more limiting for the aft centre of gravity. The forward centre of gravity limit which results from the controllability constraints is unchanged as the control stall constraint remains the limiting constraint. In fact, the control capacity required to rotate the aircraft in takeoff becomes less significant as will be discussed in Section 5.2.2.

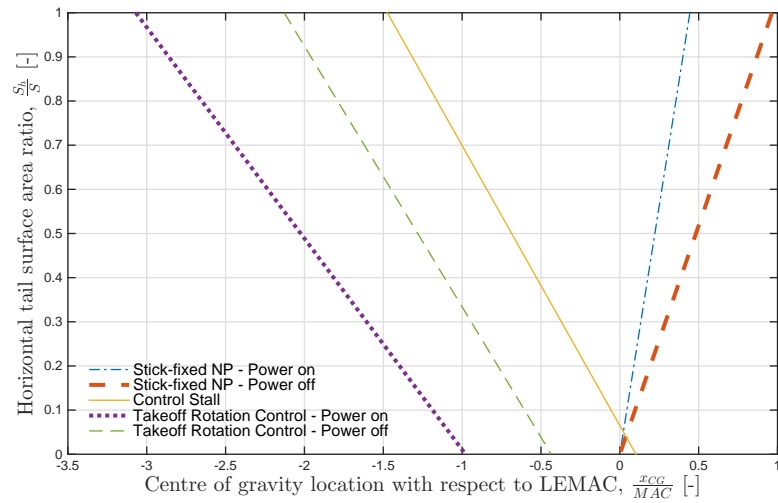


Figure 5.12: X-Plot results for the Saab 340

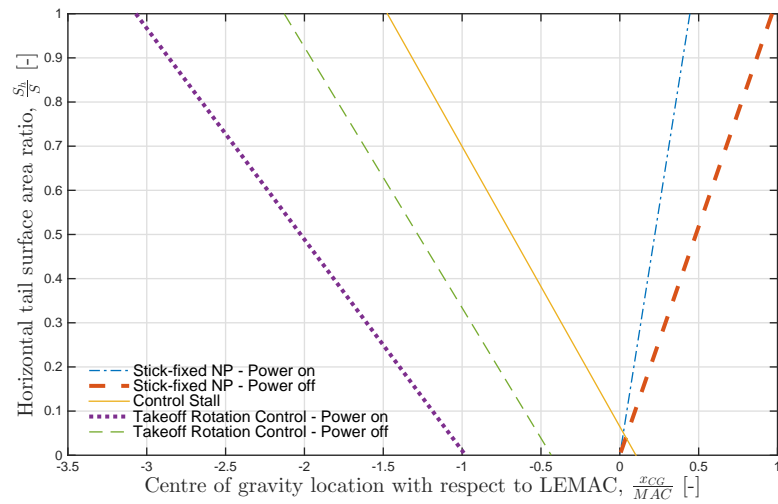


Figure 5.13: X-Plot results for the Fokker 50

FOKKER 50

Figure 5.13 shows the x-plot based on the Fokker 50 in the power off and power on condition. The figure shows similar results as the Saab 340 with the constraints shifting in the same directions. However, the shift due to

Table 5.1: Initiator design convergence dimensions compared to actual Fokker 50 dimensions

Dimension	Actual Fokker 50	Initiator Fokker 50	Difference
Fuselage Length [m]	25.25	24.1	-4.5%
Wing Area [m^2]	70	86.3	-2.4%
Wing Span [m]	29	28.6	-1.3%
Propeller Diameter [m]	3.66	3.64	-0.4%

rotating propellers is larger. This coincides with the relatively larger change in horizontal tail contribution due to the low tail position as will be described in Section 5.2.2

5.2. DISCUSSION

This discussion is split up in two major parts. First, the implemented methodology is validated by comparing the Initiator results with the corresponding wind tunnel test data [28] [10]. This validation will be carried out based on the figures found in Subsections 5.1.1 and 5.1.2. Secondly, the effect of the propeller slipstream on the longitudinal stability and control variables will be analyzed. This effect will be discussed using all the results given in the previous Section.

5.2.1. VALIDATION

The only readily available validation data that could be found are the wind tunnel test results for the tail-off lift coefficient and the pitching moment shown in Figures 5.1-5.8b. As such, these are the only figures that will be discussed here starting with the tail-off lift coefficient. It is important to reiterate here that the Saab 340 results were found using direct inputs for the dimensions of the aircraft, whereas the Fokker 50 dimensions were determined using the Initiator design convergence. The dimensions which result from the design convergence in the Initiator for the Fokker 50, as well as the actual Fokker 50 dimensions, are shown in Table 5.1.

Table 5.1 shows that the implemented methodology for the wing and engine sizing using propeller engines described in Section 3.2 gives fairly accurate results. Especially the propeller diameter prediction, which follows from the maximum tip speed, is very accurate. This does not mean that an elaborate engine sizing module is not recommended as such a module may improve the accuracy or flexibility of the engine sizing further.

TAIL-OFF LIFT CURVES - SAAB 340

Following the structure used in Section 5.1, the Saab 340 results are discussed first. Starting with Figure 5.1, the results show a good correlation with the wind tunnel test results with a maximum discrepancy of 11% in lift coefficient occurring for the the 40 degrees flap deflection case.

The main error in all three flight settings is that the lift curve slope is slightly steeper compared to the test data, leading to a lower lift coefficient at negative angles of attack and higher lift at positive angles of attack. The exact reason for this is difficult to discern, as many errors may cause this. First is the fact that the power-off lift curve slope may be too steep. This lift curve slope is predicted using @AVLVM which is based on the wings only, leading to an unavoidable error margin.

Another potential error is that the propeller normal force slope $\left(C'_{N_{\alpha_{pn}}}\right)$, calculated based on the methodology in Section 3.4.2 Equation 3.11, is slightly too large. This could be due to the fact that propeller blade chords, which are used to determine the propeller normal force, are based on the Dowty Rotol six bladed propeller used on the Fokker 50 because the propeller chords for the Saab 340 could not be found.

Finally, the lift curve slope due to slipstream, determined using the methodology in Section 3.4.3 may be over predicted. This over prediction could be due to an incorrect effective lift curve slope of the slipstream section of the wing $\left(C_{L_{\alpha, \text{eff}}}\right)$ in Equation 3.25 or a slightly steeper downwash slope $\left(\frac{d\varepsilon}{d\alpha}\right)$ causing an overpredicted downwash angle in Equation 3.24.

However, it remains difficult to ascertain the exact origin of the small error based on this figure alone. Figure

5.2 is more useful in this regard. It shows the power-on lift curves as well as the power-off lift curves. From this figure, the conclusion can be drawn that the lift curve slope as predicted by @AVLVL M is correct, albeit with a constant offset. This means that the slope must be too steep based on either the incorrect propeller normal force slope, or the slipstream section lift slope. Unfortunately, without a more detailed breakdown of validation data which quantifies each component, it is impossible to determine where the exact error lies.

However, it should still be noted that the error that occurs is very small, and the implemented method still predicts the effect of the propeller slipstream on the tail-off lift coefficient to a satisfactory degree.

TAIL-OFF LIFT CURVES - FOKKER 50

The curves for the Fokker 50 show similar effects as the Saab 340. In general, the calculated values coincide reasonably well with the measured values. However, a relatively larger error does seem to occur compared to the Saab 340.

This error was originally expected however as the Fokker 50 calculations are based on the aircraft dimensions which follow from the Initiator design convergence as mentioned earlier. This increased error is shown when comparing the power-off lift curves of Figures 5.3-5.6 to the power-off lift curve of the Saab 340. The Saab 340 lift as predicted by @AVLVL M is almost precisely the same as the wind tunnel data. Whereas the Fokker 50 power-off curves all have a larger discrepancy. This is however inherent to the Initiator design tool in that an aircraft design that follows from it does not have to be exactly the same as the reference aircraft used for the initial inputs, as previously shown in Table 5.1.

When comparing the propeller slipstream contributions, the calculations seem to slightly over predict the effect. This can be seen as the calculated curves increase relatively compared to the measured curves. Although this means that the calculated values correlate better with the measured values in some cases (Figure 5.6), this does not mean that this is correct. The over prediction is in line with the results for the Saab 340, and could thus be credited to a number of effects. Such as an erroneous increase in propeller normal force or incorrect effective lift slope for the slipstream section as mentioned earlier.

Further wind tunnel data would be needed to pinpoint the exact error. Despite the slight error in these figures, the overall method still seems to hold up well and estimates the tail-off lift coefficient with rotating propellers sufficiently well.

PITCHING MOMENT CURVES - SAAB 340

The pitching moment curves for the Saab 340 were determined by calculating the lift coefficients and pitching moments at various angles of attack. As a result, the curves are bound to have a larger error than the tail-off lift curves as the tail-off lift error is included in the figures.

Starting off by examining the tail-off pitching moments, the implemented method using the AVL input seems to follow the trend of the wind tunnel results well. In fact, the overprediction of the AVL input compared to the wind tunnel data mentioned earlier in Figure 5.2, seems to increase the accuracy of the propeller slipstream prediction. This can be seen when comparing the method; AVL input curves with the method; wind tunnel data input curves. This suggests that the implemented calculation is underpredicting the change in pitching moment. However, this underprediction is being compensated by a slight overprediction in lift by @AVLVL M. The maximum error for the tail-off pitching moment is less than 10% and as such the implemented method still adequately predicts the pitching moment in the conceptual design phase.

The tail-on pitching moments show the largest error of the validation results thus far. This error occurs due to a number of reasons. First is that the tail-on pitching moment is computed using many variables calculated previously, which means that any previous errors are included in it. Secondly, as mentioned in Section 3.4.5, the assumption is made that the downwash due to propeller slipstream is caused only by the lift increase over the wing due to the slipstream. Although this assumption seems valid, it remains a simplification which could lead to inherent inconsistencies. Finally, the implemented downwash prediction is based on @AVLVL M computations which also contain minor errors as shown in the thesis work of Jansen [6].

Despite these errors, the implemented method using AVL input still predicts the tail-on pitching moment

Table 5.2: Calculated Tail-off lift coefficients for the Saab 340 with flaps deflected 20 degrees and thrust coefficient of 0.6

Angle of Attack α [deg]	-4	0	4	8
Power-off lift C_{LP-O} [-]	0.574	0.971	1.344	1.690
Total Power-on lift C_L [-]	0.824	1.344	1.839	2.305
Wing lift minus slipstream C_{LW-S} [-]	0.558	0.945	1.308	1.645
Lift due to slipstream C_{LS} [-]	0.306	0.381	0.458	0.528
Propeller Normal Force C_{LP} [-]	0.004	0.017	0.030	0.043
Vertical thrust component C_{LT} [-]	-0.045	0	0.045	0.090

more accurately than the method using wind tunnel inputs. It should be noted that this may not be the case for every aircraft type and more validation data is needed. This again shows that the implemented methodology contains assumptions which are not completely accurate. However, these assumptions are required to have a fast prediction method in the conceptual design phase rather than computationally expensive CFD calculations or wind tunnel tests.

PITCHING MOMENT CURVES - FOKKER 50

The tail-off pitching moment curves for the Fokker 50 show a similar trend as for the Saab 340. The change in pitching moment due to propeller thrust is slightly underpredicted, especially at higher flap deflections, but still follows the trend reasonably well. The fact that the error increases for higher flap deflections indicates that the flap lift prediction by @AVLVLM is not entirely correct. Which is an expected result as AVL only predicts a plain flap system, rather than more advanced flap systems typically implemented. This can be improved when the @HighLiftSystems module is reintegrated in the Initiator. For now however, the pitching moment due to rotating propellers using the implemented methodology seems to be predicted well.

5.2.2. ANALYSIS

In this subsection, the effect of rotating propellers on the entire longitudinal stability and control will be discussed, starting with the tail-off lift coefficient up until the complete effect of all the changing variables on the x-plot.

TAIL-OFF LIFT COEFFICIENT

Figures 5.1-5.6 all clearly show the total effect of rotating propellers on the tail-off lift coefficient as calculated. This total effect is an increase in lift coefficient seen as steeper lift curve slopes for higher thrust coefficients. To analyze the change in lift coefficient quantitatively, a breakdown is given in Table 5.2 of the total tail-off lift coefficient as calculated for Figure 5.2. This breakdown lists the four variables calculated as described in Section 3.4.3 for four different angles of attack as well as the power-off and total power-on lift coefficient.

This table shows some interesting results. First is that the total lift coefficient is increased by an average of 38% with respect to the power-off lift coefficient. This could also be seen from Figure 5.2 and clearly confirms the importance of determining the propeller slipstream effect whilst designing a propeller aircraft.

Another important result from Table 5.2 is the fact that the majority (a minimum of 78% at an 8 degrees angle of attack) of the lift increase due to propeller thrust is caused by the increased flow velocity over the slipstream section of the wing (C_{LS}). In fact, at -4 degrees angle of attack, the lift due to slipstream is responsible for 116% of the increase in lift because the vertical thrust is directed downwards at this negative angle of attack. This also proves that the one engine inoperative case in take-off can have drastic results if not taken into account during the design phase. With one engine inoperative, the lift over only side of the wing increases, causing the aircraft to roll. Unfortunately, the directional stability could not be examined as part of

this thesis and a prediction model for this needs to be implemented within the Initiator.

One final result that is important to analyze is the fact that, as expected, the increase in lift is proportionate to the propeller thrust coefficient. This means that the propeller slipstream effect will be strongest during take-off, where the thrust is maximum due to the low aircraft velocity as described in Section 2.1.

PITCHING MOMENT COEFFICIENT

Figures 5.7a-5.8b all show the pitching moment on the x-axis as well as the lift coefficient on the y-axis. Focusing on the pitching moment, the tail-off pitching moment becomes more negative (nose down) due to rotating propellers according to the calculations and wind tunnel measurements. The pitching moment becomes more nose down because the increase in lift over the slipstream section is applied aft of the moment reference centre.

Interestingly, the effect of propeller thrust reduces for higher angles of attack. At higher angles of attack, the positive pitching moment caused by the propeller normal force and the upwash caused by the fuselage and nacelles reduce the nose down pitching moment effect. In fact, at even higher angles of attack, the effect may become positive.

Furthermore, the effect explained above becomes stronger for higher thrust coefficients as expected, but also for higher flap deflections. The flap deflection has an influence due to the fact that deflected flaps cause the increase in lift over the slipstream section of the wing to become larger and that the point of application of the lift on the wing moves further back as explained in Section 3.4.4.

In terms of the tail-on pitching moment, the increase in downwash due to the propeller slipstream causes tail contribution to become more nose up as the effective angle of attack of the tail is reduced. This effect is not shown however in these figures as no complete power-off pitching moments were measured. Instead, Figures 5.9a - 5.11a show the tail contribution as calculated.

TAIL CONTRIBUTION

Figures 5.9a-5.11a all show the tail contribution to the pitching moment versus angle of attack. As mentioned earlier, the tail height has a significant influence on the pitching moment. To clearly describe the influence of tail location, the tail pitching moment contribution equation detailed in Section 3.4.5 is repeated below:

$$\Delta C_{m_h} = -C_{L_{\alpha,h}} \tilde{V}_h (\alpha_r - \varepsilon + i_h) \frac{q_h}{q} \quad (5.1)$$

Using this equation for the Saab 340 with a T-tail configuration gave a negative linear curve for the power-off and power-on conditions. As the distance between the tail and the slipstream centre line in the power-on condition is greater than the contracted propeller slipstream diameter, no nonlinear inflow effects on the downwash or dynamic pressure increases occur. Because no inflow effects occur, the variation in downwash is only dependent on the lift coefficient which varies linearly with respect to the angle of attack as shown in Figures 5.1. Furthermore, as explained previously, the lift coefficient increases for increasing propeller thrust, resulting in a higher downwash. Because of this, the tail experiences a lower effective angle of attack ($\alpha_r - \varepsilon + i_h$). The lower effective angle of attack reduces the effectiveness of the tail due to a reduction in stabilizing negative (nose-down) pitching moment at higher angles of attack.

The Fokker 50 results are slightly more complicated. Whilst the power-off results are similar to the Saab 340, the power-on results vary non-linearly with the angle of attack due to the inflow effect and dynamic pressure increase.

The inflow effect, described earlier in Section 3.4.5, is the inflow of the outer flow into the propeller slipstream as sketched in Figure 3.14. This inflow effect occurs in the mixing region on the boundary of the contracted slipstream tube. This effect was approximated by Obert [10] to the non-linear curve in Figure 3.15. As the angle of attack in Figures 5.10a-5.11a increases, the vertical distance between the tail and slipstream centre line (h_{tot}) changes. Thus, the average downwash due to inflow also changes. In all three figures, this effect increases the downwash, resulting in a less effective horizontal tail.

Specifically, the maximum average downwash due to inflow occurs at different angles of attack for the three flap deflections as indicated in the figures. This is the case because the vertical distance h_{tot} is dependent on the flap deflection as increased flaps deflect the slipstream centre line further downwards. After the maximum average downwash due to inflow has been reached, the total downwash versus angle of attack slope $\left(\frac{\delta \varepsilon}{\delta \alpha}\right)$ decreases. This slope decrease can be seen in the figures as an increase in tail effectiveness.

The average dynamic pressure, also described in Section 3.4.5, is a function of the previously mentioned h_{tot} and the ratio between the slipstream diameter and the tail span. An increase in dynamic pressure at the tail increases the lift over the tail. It follows naturally that an increase in dynamic pressure thus increases the effectiveness of the horizontal tail. This can be seen through a steeper tail pitching moment curve. For the three flap deflection figures shown, the maximum dynamic pressure ratio occurs for the case with the flaps retracted. With flaps retracted, the slipstream centre line is not deflected by the flaps, and the vertical distance h_{tot} is lowest.

In terms of effectiveness, the tail is most effective with the flaps retracted as can be seen from the steep curve. This case is most effective due to two reasons. The first reason is that the previously mentioned highest dynamic pressure ratio increases the lift produced by the tail more than the flaps deflected cases. Secondly, as the downwash is lower, the effective angle of attack at the horizontal tail is higher.

EFFECT ON TAIL SIZING

The effect of rotating propellers on tail sizing is shown in Figures 5.12 and 5.13. In the figures, the aft centre of gravity limit due to the stick-fixed stability requirements is shown as well as the forward centre of gravity limit due to two controllability requirements.

First examining the stick-fixed stability, the propeller slipstream has a negative effect on the longitudinal stability of the aircraft and tail sizing. This is clearly indicated in the figures as the power on curves for both aircraft are steeper. These steeper curves indicate that for the same horizontal surface area, the power on condition reduces the allowable aft centre of gravity position. This shift occurs due to the reduced tail contribution described in the previous subsection. This also explains why the effect is worse for the Fokker 50 than for the Saab 340. The Fokker 50 has a low wing configuration, which as previously discussed, causes an additional increase in downwash due to rotating propeller by the inflow effect, resulting in reduced tail effectiveness.

Contrary to the stick-fixed stability, the control capacity limit for the takeoff rotation is actually relaxed due to propeller power. As can be seen, the allowable forward centre of gravity for a certain tail surface area ratio is further forward for the power-on condition than the power-off condition. The reasoning for this is twofold. First, the downwash at the horizontal tail is increased. This increase in downwash causes the effective angle of attack of the tail to be lower, which leads to a larger negative lift caused by the elevator. This negative lift causes an increased nose up pitching moment, which is required to rotate the aircraft. Interestingly enough, this means that an increase in downwash, which is detrimental for the longitudinal stability, has a positive effect on the takeoff rotation controllability. The second reason, which is only valid for low wing aircraft, is the increased dynamic pressure over the horizontal tail. This increased dynamic pressure further increases the lift over the tail, thus increasing the pitch up moment further. This effect can be seen when comparing both figures as the shift due to the power-on condition is larger for the Fokker 50.

Although the takeoff rotation limit is relaxed, the forward centre of gravity limit does not change. This is due to the fact that the control capacity required to stall the aircraft is still the dominant limit for the forward centre of gravity. As discussed earlier, the assumption was made that the engines were idle in the landing configuration. This assumption means that forward centre of gravity limit does not affect the dominant forward centre of gravity limit.

Overall, this means that the horizontal tail size should increase based on the fact that the stick-fixed stability is reduced due to the propeller slipstream effect. However, as this was only checked for these three constraints, and only for the default wing position, it is important to note that the exact change in tail size is impossible to ascertain at this time. As soon as the *@HorizontalStabilityEstimation* module work is completed, this methodology can be incorporated and qualitative results can be found.

6

CONCLUSIONS

The research objective was defined in the Introduction as: 'Develop, implement, and validate a prediction method for the propeller slipstream effect on the longitudinal stability and control in the conceptual design phase of conventional aircraft configurations. In developing this method, the effect of the propeller slipstream was investigated. During this investigation, it was discovered that the implementation of propeller engines causes four major effects on the longitudinal stability and control of an aircraft. These are, an additional normal force at the propeller disk, an increase in lift over the wing due to the slipstream, a change in the tail-off pitching moment, and a change in tail contribution to the pitching moment.

Following this investigation, a method was implemented into the Initiator which rapidly predicts these four major effects. This semi-empirical method was validated using data found for the Fokker 50 and Saab 340. The validation showed an overall good agreement between the method and validation data for the tail-off lift and pitching moments.

Following an analysis of the results obtained using the method, the following conclusions could be drawn in terms of propeller slipstream effect:

- The increase in tail-off lift due to propeller engines is primarily caused by the increase in flow velocity over the wing slipstream section.
- The tail-off pitching moment becomes more negative due to rotating propellers
- The shift in tail-off pitching moment is far less significant at higher angles of attack because the propeller normal force increases
- The downwash slope at the horizontal tail is increased due to the increase in lift, reducing the tail effectiveness
- For low tail configurations, the downwash is further increased when the tail is positioned near the slipstream tube through an inflow effect
- For low tail configurations, the dynamic pressure is also increased as the tail if the tail is positioned within the slipstream. This dynamic pressure increases the tail effectiveness

Finally, the tail sizing based on three longitudinal stability and controllability constraints lead to the following conclusions:

- The implementation of propeller engines has a negative influence on the stability of an aircraft as the effectiveness of the tail is reduced
- The implementation of propeller engines has a positive influence on the control capacity required to rotate an aircraft during takeoff due to the increased downwash increasing the positive pitching moment required from the tail

7

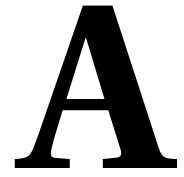
RECOMMENDATIONS

Following the conclusion of this thesis work, a number of recommendations can be made to continue this research. These recommendations are split into two parts. The first group of recommendations are related to the overall implementation of propeller engines within the Initiator. The second group of recommendations are related to the implemented prediction method for the propeller slipstream effect on the longitudinal stability and control.

As part of this thesis, a basic implementation of propeller engines was entered in the Initiator. However, this implementation can be significantly improved. The first recommendation is that during the actual code integration into the Initiator, this work needs to be carefully compared with the work of van Bogaert [22] mentioned earlier in Chapter 4 to ensure no overlapping occurs. Secondly, many modules can be built to expand on this basic implementation. For instance, an actual engine model can be built which accurately calculates the fuel consumption based on the altitude, velocity and power setting. Furthermore, this engine model could include propeller sizing to accurately determine propeller blade section chords required for the propeller normal force prediction. Additionally, additional propeller effects which have currently not been implemented yet can be investigated. Examples of these effects are, the influence of the propeller slipstream effect on the directional and lateral stability and control, difference in thrust and drag bookkeeping due to swirl recovery, propeller influence on noise, and the influence of fuselage-mounted propeller engines.

In terms of improvements to the implemented prediction method, the main work to be done consists of reducing the number of assumptions made in this method. The assumptions made in this method enabled its development and allow for the rapid computations. However, some assumptions also lead to inherently false results. For instance, the assumption that no deformation of the stream tube or mixing with the outer flow occurs, is rather bold and it directly affects the calculation of the dynamic pressure of the tail. Instead of this assumption, additional research could be done to investigate the deformation of the stream tube and determine whether it is possible to model this deformation without using extensive CFD calculations.

One final important recommendation is to obtain more validation data through wind tunnel tests into the propeller slipstream effect. This additional data could be used to further validate the implemented method and allow for future improvements to the method to be developed.



SAAB 340 AND FOKKER 50 DIMENSIONS

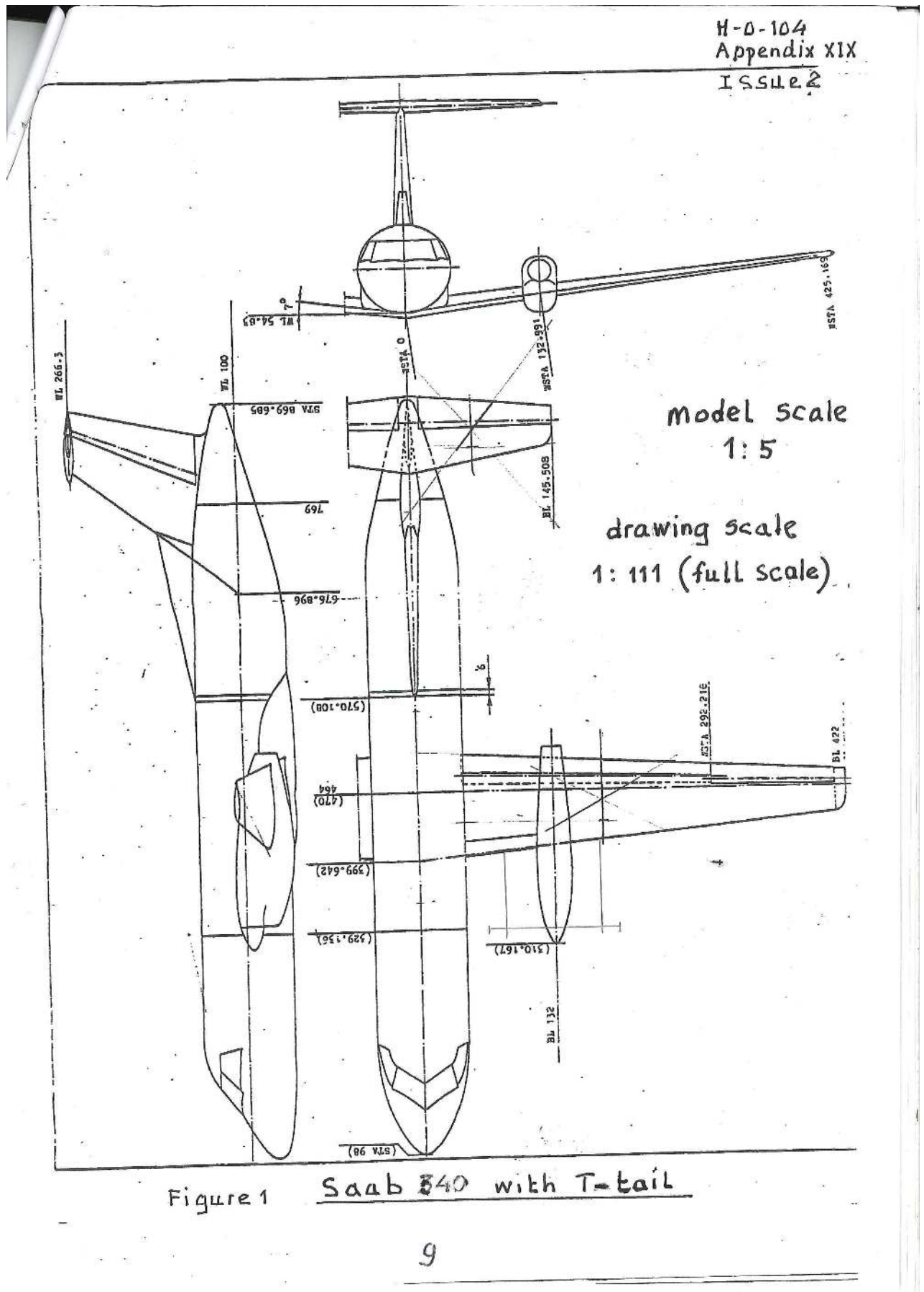


Figure A.1: Saab 340 dimensions

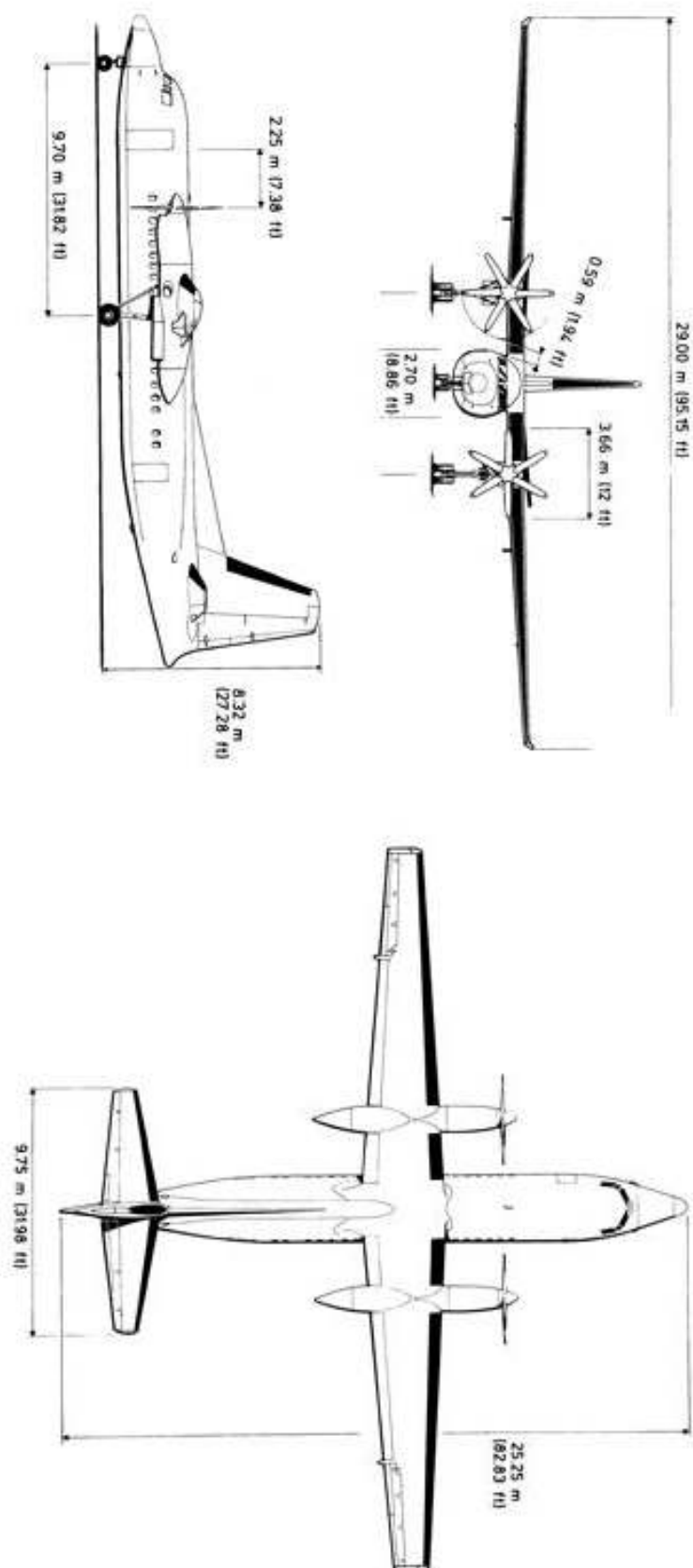


Figure A.2: Fokker 50 dimension

BIBLIOGRAPHY

- [1] E. Obert, R. Slingerland, D. Leusink, T. van den Berg, J. Koning, and M. van Tooren, *Aerodynamic Design of Transport Aircraft* (Ios Press, 2009) ISBN:9781586039707.
- [2] J. Roskam and C. Lan, *Airplane Aerodynamics and Performance* (Design, Analysis and Research Corporation, 1997) ISBN = 9781884885440.
- [3] L. Veldhuis, *Propeller wing aerodynamic interference* (TU Delft, Delft University of Technology, 2005) ISBN:9090195378.
- [4] E. Torenbeek, *Synthesis of Subsonic Airplane Design* (Delft University Press, 1982) ISBN:9789401732024.
- [5] E. R.J.M., *Synthesis of Novel Aircraft Concepts for Future Air Travel*, Thesis.
- [6] Q. Jansen, *Relaxed Static Stability Performance Assessment on Conventional and Unconventional Aircraft Configurations*, Thesis (2015).
- [7] U. Government, *Flight Training Handbook* (Pgw, 1988) ISBN:9781560270058.
- [8] J. De Young, *Propeller at high incidence*, Journal of Aircraft **2**, 241 (1965), ISSN:0021-8669.
- [9] J. Campbell and M. McKinney, *NACA Report 1098 - Summary of Methods for Calculating Dynamic Lateral Stability and Response and for Estimating Lateral Stability Derivatives*, Report (National Advisory Committee for Aeronautics).
- [10] E. Obert, *A method for the determination of the effect of propeller slipstream on the static longitudinal stability and control of multi-engined aircraft* (Delft University Press, 1997).
- [11] W. Phillips, *Mechanics of Flight* (Wiley, 2004) ISBN:9780471334583.
- [12] T. Theodorsen, *The theory of propellers - part iii, the slipstream contraction with numerical values for two-blade and four blade propellers*, NACA Report **777** (1944).
- [13] M. Hoogreef, *Initiator manual*, <http://fppwiki.lr.tudelft.nl/index.php/Synthesis/Initiator>.
- [14] T. Langen, *Development of a conceptual design tool for conventional and boxwing aircraft*, Thesis (2011).
- [15] D. Raymer, *Aircraft Design: A Conceptual Approach* (AmerInst of Aeronautics, 2013) ISBN: 9781600869211.
- [16] A. Elham, *Weight Indexing for Multidisciplinary Design Optimization of Lifting Surfaces*, Thesis (2008).
- [17] J. Roskam, *Airplane Design: Part 1* (DARcorporation, 1985) ISBN:9781884885426.
- [18] J. Hunter, *Jane's All the World's Aircraft: In Service 2014-2015: Yearbook* (Jane's Information Group, 2014) ISBN:9780710630940.
- [19] M. Drela and H. Youngren, *xrator*, (2003), <http://web.mit.edu/drela/Public/web/xrator/>.
- [20] G. Ruijgrok, *Elements of Airplane Performance* (Delft University Press, 1990) ISBN:9789062756087.
- [21] Z. Spakovsky, *Performance of propellers*, <http://web.mit.edu/16.unified/www/FALL/thermodynamics/notes/node86.html>.
- [22] J. van Bogaert, *Assessment of Potential Fuel Saving Benefits of Hybrid-Electric Regional Aircraft*, Thesis (2015).

- [23] H. S. Ribner, *Propellers in yaw* (National Advisory Committee for Aeronautics, 1943).
- [24] E. S. D. Unit, *Propeller slipstream packages* (IHS, 1986) ISBN:9780856795213.
- [25] B. Munniksma, *N-250 propeller shop test report*, (1990).
- [26] W. Stepniewski, *Expérience tirée des essais en vol d'un appareil VTOL a aile basculante*. Technique et Science Aeronautiques **No. 1** (1960).
- [27] M. Drela and H. Youngren, *Athena vortex lattice*, (2010).
- [28] E. Obert, *The effect of propeller slipstream on the longitudinal characteristics of a model of the saab 340 with a t-tail*, (2015).
- [29] H. Glauert, *Theoretical relationships for an airfoil with hinged flap*, ARC R M 1927 **No. 1603** (1934).
- [30] *Airfoil tools*, <http://airfoiltools.com/index>.
- [31] D. Lednicer, *The incomplete guide to airfoil usage*, (2010), <http://m-selig.ae.illinois.edu/ads/aircraft.html>.
- [32] MathWorks, *Matlab*, (2014), <http://nl.mathworks.com/products/matlab>.